





Original Article


Geomorphic and tectonic controls of landslides induced by the 2022 Luding earthquake


ZHAO Bo¹  <https://orcid.org/0000-0002-2565-8752>; e-mail: zhaobo1989@imde.ac.cn


HU Kai-heng¹  <https://orcid.org/0000-0001-8114-5743>; e-mail: khhu@imde.ac.cn


YANG Zong-ji¹  <https://orcid.org/0000-0003-4108-2092>; e-mail: yzj@imde.ac.cn


LIU Qiao¹  <https://orcid.org/0000-0002-7285-5425>; e-mail: liuqiao@imde.ac.cn



ZOU Qiang¹  <https://orcid.org/0000-0003-0029-8532>; e-mail: zouqiang@imde.ac.cn

CHEN Hua-yong¹  <https://orcid.org/0000-0003-4033-3339>; e-mail: hychen@imde.ac.cn

ZHANG Bo¹  <https://orcid.org/0000-0002-7056-1124>; e-mail: rsbozh@imde.ac.cn

ZHANG Wei-feng¹  <https://orcid.org/0000-0002-3333-7174>; e-mail: zwf@imde.ac.cn

ZHU Lei¹  <https://orcid.org/0000-0003-3199-0054>; e-mail: zhul@imde.ac.cn

SU Li-jun^{1,2,3*}  <https://orcid.org/0000-0001-9972-4698>;  e-mail: sulijun1976@163.com

*Corresponding author

¹ Institute of Mountain Hazards and Environment, Chinese Academy of Sciences, Chengdu 610041, China

² China-Pakistan Joint Research Center on Earth Sciences, Islamabad 45320, Pakistan

³ University of Chinese Academy of Sciences, Beijing 100049, China

Citation: Zhao B, Hu KH, Yang ZJ, et al. (2022) Geomorphic and tectonic controls of landslides induced by the 2022 Luding earthquake. *Journal of Mountain Science* 19(12). <https://doi.org/10.1007/s11629-022-7732-8>

© Science Press, Institute of Mountain Hazards and Environment, CAS and Springer-Verlag GmbH Germany, part of Springer Nature 2022

Abstract: On 05 September 2022, an Ms 6.8 (Mw 6.6) earthquake occurred in Luding County, Sichuan Province, China, with the epicenter at 29.59°N, 102.08°E and a focal depth of approximately 16.0 km. Combining field investigations, high-resolution satellite images and multiple datatypes characterizing the seismogenic structure, topography and geology, this study attempts to discuss the influence of geomorphic and tectonic indexes on landslide distribution. The results show that the 2022 Luding earthquake with seismogenic fault at the Moxi fault, was a sinistral

strike-slip event that triggered at least 4528 landslides over an area of ~2000 km². These landslides span a total area of 28.1 km², and the western section of the seismogenic fault, which serves as the active wall area, is characterized by a higher landslide concentration, especially in the Wandong Basin. The seismogenic fault and lithology influence the regional distribution of landslides, and more landslides occurred closer to the seismogenic fault and in the controlling lithologies of granite and dolomite. Local topography influences the landslide occurrence position on the slope; the eastern section is prone to form landslides in the lower gorge section, and the western section is prone to form landslides in

Received: 24-Sep-2022

Revised: 20-Oct-2022

Accepted: 09-Nov-2022

the upper-top section of the gorge. For coseismic landslides in the eastern Baryan Har block, the eastern boundary (Longmenshan fault), where the earthquakes are characterized by thrusts with slight dextral strike-slip movement, could be the primary landslide-prone area; the southern boundary, the Moxi fault and the southern segment of the Xianshuihe fault, with more intensive strike-slip movement, may be the secondary landslide-prone area; and the northern boundary is the tertiary landslide-prone area. Additionally, the current landslide inventory may be underestimated although this underestimation has limited influence on the results.

Keywords: Landslides; Luding earthquake; Spatial distribution; Geomorphic index; Tectonic index

1 Introduction

Earthquakes, caused by the sudden release of energy from Earth's lithosphere, can cause strong shaking of the surface of the Earth and thus massive rock masses to detach from mountains, forming earthquake-triggered landslides; earthquake-triggered landslides are usually called seismic or coseismic landslides (Keefer 1984, 2002; Stein and Wysession 2009; Harp et al. 2011; Huang and Fan 2013; Tanyaş et al. 2017; Fan et al. 2019). It is widely accepted that individual seismic events are capable of regionally triggering landslides, and these coseismic landslides shape the regional topography and serve as important agents of landscape evolution, especially in seismically active mountainous areas (Ren et al. 2014; Kargel et al. 2016; Roback et al. 2018; Wang et al. 2020). Some studies have indicated that coseismic mass wasting may restrict mountain growth (Parker et al. 2011).

Numerous studies have reported that the Qinghai-Tibet Plateau could be a typical coseismic landslide-prone area, especially the eastern margin (Xu et al. 2014a, 2015; Fan et al. 2018; Zhao et al. 2022b). The high geostress, deep-cutting gorges, densely distributed faults and fractures, etc., make the eastern margin very sensitive to earthquakes, and slight shaking may cause rock slope failures (Zhao 2020). For example, since 2000, at least 7 earthquakes have triggered massive landslides on the eastern margin, including the 2008 Mw 7.9 Wenchuan (197481 landslides), 2010 Mw 6.9 Yushu

(2036 landslides), 2013 Mw 5.5 Minxian (6478 landslides), 2013 Mw 6.6 Lushan (15645 landslides), 2014 Mw 6.2 Ludian (1414 landslides), 2017 Mw 6.5 Jiuzhaigou (5633 landslides), and 2022 Mw 5.8 Lushan (1288 landslides) earthquakes (Xu et al. 2014a, 2014b, 2015; Tian et al. 2019; Zhao et al. 2022b). These coseismic landslides bring catastrophic consequences for locals, such as village submergence, fatalities and lake damming (Zhao et al. 2022b).

Before evaluating spatial and size distribution of coseismic landslides triggered by one seismic event, it could be essential to establish a complete inventory as it could provide the basic ground truth for landslide analysis and assessment (Guzzetti et al. 2012; Xu 2015). Some relative analysis, such as Kernel density distribution, size distribution, influence of seismogenic fault, rocks, river, elevation, slope, local relief and aspect on landslide distribution, were carried out (Keefer 1984; Fan et al. 2019). Some basic laws were also accepted generally, such as the landslide-affected area, landslide size and landslide concentration generally increase with increasing earthquake magnitude (Keefer 1984; Gorum et al. 2011; Xu et al. 2014a, 2015; Fan et al. 2019; Zhao 2021; Zhao et al. 2021a, 2021b, 2022a). Not every earthquake will trigger coseismic landslides because the local geological, topographic, tectonic and climate conditions also influence landslide occurrence (Gorum et al. 2013; Kargel et al. 2016; Conforti and Ietto 2020; Zhao et al. 2022a); for example, coseismic landslides are concentrated mainly in mountainous areas featuring high local reliefs (Meunier et al. 2008; Clarke and Burbank 2010; Chen et al. 2011; Jeandet et al. 2019; Medwedeff et al. 2020), and fractured rock may be more susceptible to the occurrence of coseismic landslides (Pradhan et al. 2006; Owen et al. 2008; Chen et al. 2012). Thus, enhancing the understanding of coseismic landslides triggered by individual seismic events could provide valuable information for further geohazard assessment and evidence of the relationship between tectonics and geohazards (Roback et al. 2018; Fan et al. 2019; Zhao et al. 2020a).

On 05 September 2022, 12:52 (Beijing time), an Ms 6.8 (Mw 6.6) earthquake, later called the Luding earthquake, struck Luding County, Sichuan Province, China, with an epicenter at 29.59°N, 102.08°E and a focal depth of approximately 16.0 km (CENC 2022); the event caused 93 casualties (before 12 September) and severe infrastructure damage (CCTV 2022).

Additionally, this earthquake caused numerous landslides; thus, this study attempts to explore the possible influences of seismogenic structure, topography, and lithology on the regional distribution and abundance of coseismic slope failures. We also systematically compare our findings with the results of other earthquakes on the eastern margin of the Baryan Har block.

2 Seismogenic Setting

2.1 Regional setting

On 5 September 2022, a magnitude M_s 6.8 earthquake, named the 2022 Luding earthquake, struck the Xianshuihe fault zone (CENC 2022). The 2022 Luding seismic event occurred at the junction of three fault blocks: the Songpan-Ganzi fold belt (eastern margin of the Baryan Har block), Sichuan Basin (Huanan block), and Chuan-Dian block (Fig.

1A). The regional GPS velocities present a SE direction from over approximately 20 mm/yr to less than 5 mm/yr, and a considerable strain energy is concentrated in this area (Fig. 1A; Zhao et al. 2015; Wang et al. 2021).

Three active faults, namely, the Xianshuihe fault, Longmenshan fault and Anninghe fault, are located along these three block boundaries, and numerous earthquakes have occurred along these faults (Fig. 1A; Papadimitriou et al. 2004; Ran et al. 2008, 2010; Wang et al. 2014; Bai et al. 2022). The Xianshuihe fault is a NW fault with sinistral strike-slip movement and can be divided into the Luhuo (9-12 mm/yr; Wang et al. 2009), Dawu (8.12-9.30 mm/yr; Sun et al. 2021), Qianning (14-20 mm/yr; Chen et al. 2016) and Moxi (9.6-13.4 mm/yr; Bai et al. 2021) segments from north to south. The 2022 Luding seismic event occurred in the Moxi segment (Moxi fault) of the Xianshuihe fault (Fig. 1B). Since 1700, there have been 9 seismic events along the Xianshuihe fault with magnitudes ≥ 7.0 , and all of them have produced

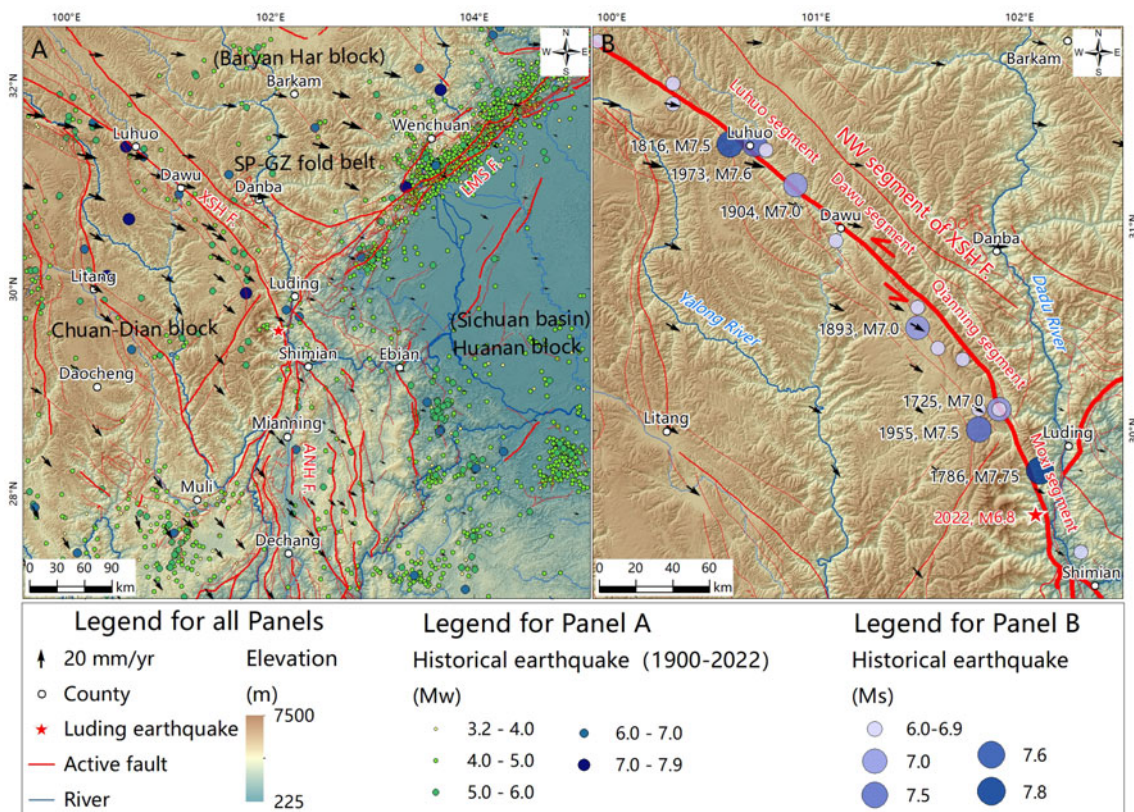


Fig. 1 Tectonic setting of the 2022 Luding seismic event. (A) Regional setting; (B) seismogenic setting. The topographic data are from a 90 m DEM (<http://www.gscloud.cn>); the active faults are from Deng et al. (2014); the GPS velocity (time period: 2009–2014, Panels A and B) is digitized from Zhao et al. (2015). Historical earthquakes (1900–2022) in Panel A are from the USGS (<https://earthquake.usgs.gov/earthquakes/map>); historical earthquakes in Panel B are from Papadimitriou et al. (2004). In Panel A, SP-GZ fold belt – Songpan-Ganzi fold belt, XSH F. – Xianshuihe fault, LMS F. – Longmenshan fault, ANN F. – Anninghe fault.

surface ruptures (Bai et al. 2022).

The 2022 Luding earthquake-affected area is located in the Shimain-Luding section (mid-downstream) of the Dadu River (Fig. 2A). The Moxi fault in this area presents an approximately N-S extension, is located in the western section of the mainstream, and crosses the subbasins of Yanzigou, Moxizigou, Hailuogou, Wandong, Changheba, Tianwan, etc. (Fig. 2A). The typical geomorphic features are deep-cutting gorges with high reliefs from 7000 m (Gongga Mountain in Fig. 2A) to less than 1000 m (Dadu River valley), and the mainstream valley usually contains two sections: a lower gorge section and a higher wide valley section (Wang et al. 2007, 2012; Wu 2013; Bai et al. 2020; Zhao et al. 2021c).

The 2022 Luding earthquake area is also an area with typically high geostress, and the maximum principal stress reaches 26 MPa and is oriented in the N50°–75°W direction (Huang et al. 2011; Wu 2013). The high geostress coupled with the rapid river incision (Luding section: 0.38 mm/yr, Zhao et al. 2013) causes rock to unload strongly toward the free space (Zhao et al. 2021c). All these factors lead to many fractures in the rocks in this area (Wang et al. 2007, 2013; Wu 2013; Zhao et al. 2021c).

The earthquake area widely covers the early Sinian granite (T1), early Proterozoic Heiyangbaozi superunit (T2), middle Triassic Leikoupo group (T3), etc.; the most common rocks include granite, dolomite, quartz diorite, and quartz sandstone (Fig. 2B).

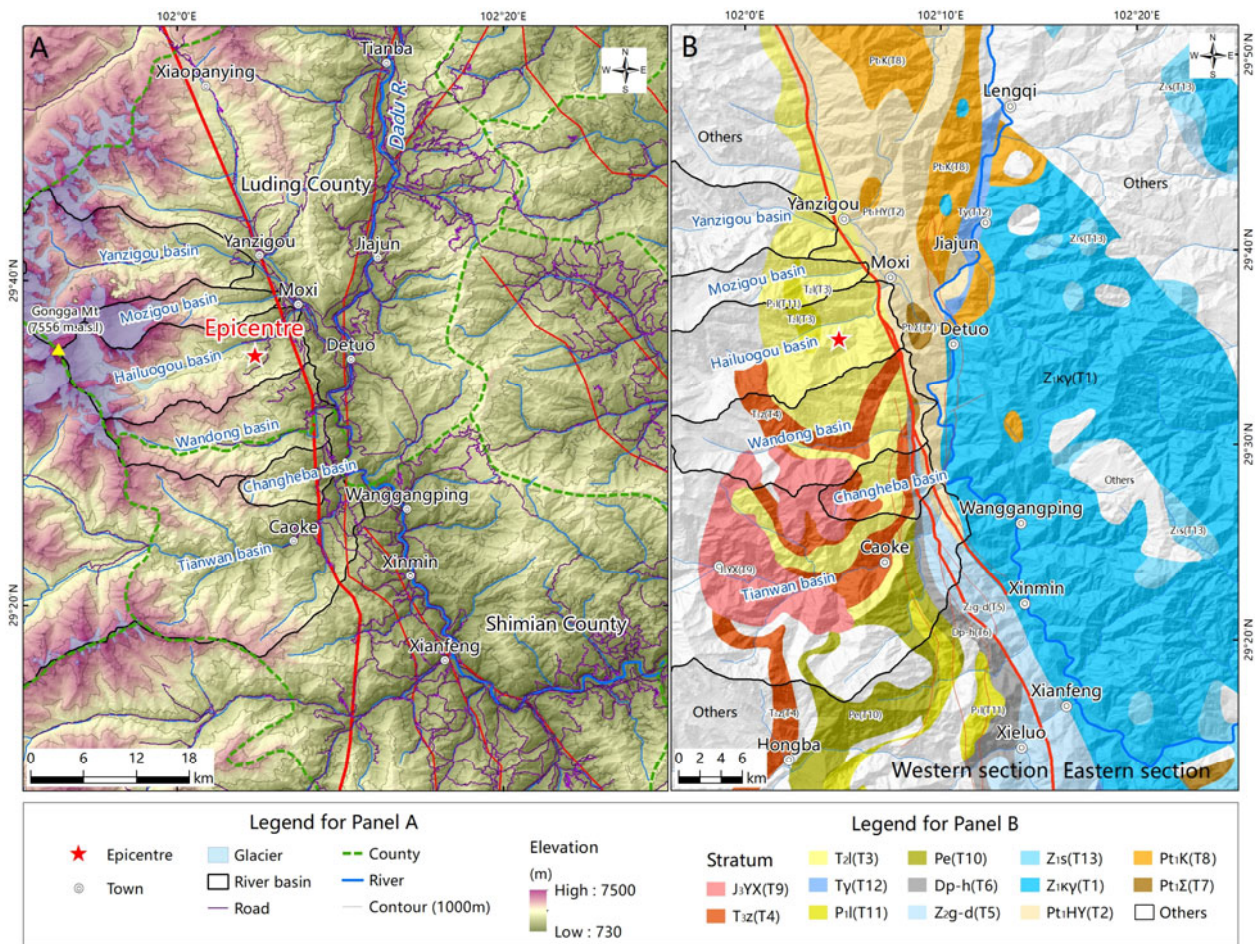


Fig. 2 Regional setting of the epicentral area. (A) Physical geographical characteristics, (B) geological characteristics. In Panel A, the geological data are digitized from a 1:50,000 geological map, and the road route is from 1:250,000 national basic geographic data (<https://www.webmap.cn/>). In Panel B, T1-T13 are stratum symbols, and T1 – early Sinian granite, T2 – early Proterozoic Heiyangbaozi superunit, T3 – middle Triassic Leikoupo group, T4 – upper Triassic Zagunao group, T5 – middle Sinian Guanyin-Dengying group, T6 – Devonian Bangda-Hexin group, T7 - Paleoproterozoic undifferentiated ultrabasic rocks, T8 – Presinian Kangding rock group, T9 – upper Jurassic Youxianping superunit, T10 – Permian Emeishan basalt, T11 – lower Permian Liangshan group, T12 – Triassic granite, T13 – lower simian Suxiong group, others belong to the stratum that no coseismic landslides occurred.

2.2 Characteristics of the 2022 Luding earthquake

The 2022 Luding seismic event occurred due to slip on the Moxi fault (southern segment of the Xianshuihe fault) in Hailuogou gully (Fig. 2). The Moxi fault is very active and is considered the seismogenic fault of the 1786 Ms 7.75 earthquake (Moxi earthquake; Dai et al. 2005; Wang et al. 2019; Zhao et al. 2021c). The 1786 Moxi earthquake triggered the Mogangling and Lantianwang landslides, and the Mogangling landslide blocked the Dadu River completely for ten days; when the dam broke, it resulted in over 100,000 casualties (Dai et al. 2005).

The focal mechanism indicates that the 2022 Luding earthquake was a strike-slip earthquake with a strike of 166° and a dip of 80° (IEF 2022a). The GNSS result shows that the southern section (near Jiulong County) underwent SSW coseismic deformation with a maximum reaching 20 mm, the eastern section of the Moxi fault (near Luding County) underwent NNE coseismic deformation, and the area near Shimian underwent NW deformation (Fig. 3A; IEF 2022b). The theoretical coseismic deformation is similar to the GNSS result (Fig. 3B; IEF 2022c). The maximum earthquake intensity reached IX degrees and was mainly concentrated between Wangangping town and Moxi town (Fig. 3A).

According to the aftershock inventory provided by the Sichuan Earthquake Administration, there were 2731 aftershocks up to 12 September 2022, 8:52:4, 56, and 387 events with magnitudes (M_s) of 4.0-5.0, 3.0-4.0 and 2.0-3.0, respectively. Additionally, three obvious areas of aftershock concentration arose in Caoke town, Gongga gully and the northern section of Yanzigou town (Fig. 3C). Additionally, the western section of the Moxi fault is the hanging wall. According to the relationships of regional GPS movements, the western section of the Moxi fault was active wall area, and the eastern section was passive wall area.

3 Material and Method

3.1 Data collection

To clarify how geology, topography, etc., influence coseismic landslide occurrence, we collected multiple remote sensing, topographic, seismic, geological, physical geographic, and field investigation datasets. For remote sensing data, we collected multiple high-resolution satellite images after the 2022 Luding event, as shown in Fig. 4. The satellite images consist of Gaofen 6 images (resolution: 8 m), Gaofen 2 images (resolution: 3.2 m) and Beijing

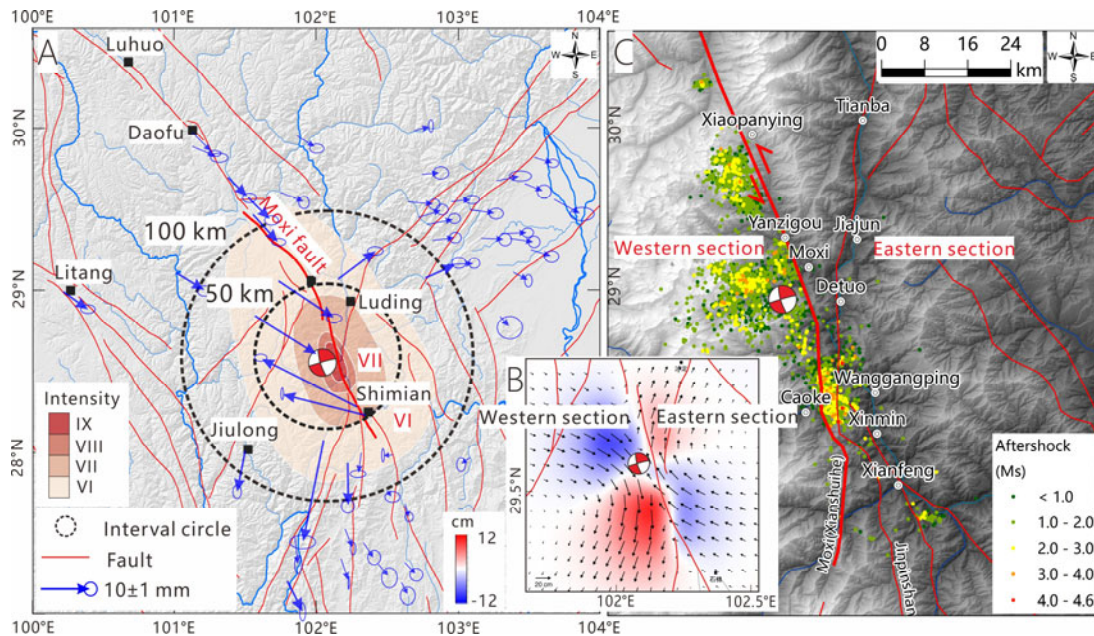


Fig. 3 Typical characteristics of the 2022 Luding seismic event. (A) Seismic intensity and monitoring coseismic deformation, (B) theoretical coseismic deformation distribution, (C) distribution of aftershocks (mainshock – 12.09.2022 8:52). The Panel A is from IEF (2022b), the Panel B is from IEF (2022c); the seismic intensity is from Ministry of Emergency Management (https://www.mem.gov.cn/xw/yjglbgzdt/202209/t20220911_422190.shtml), the aftershock inventory is provided by Prof. Shiyuan Wang from Sichuan earthquake Administration.

3 images (resolution: 2 m). These satellite images cover an area of 2×10^4 km². As plenty of satellite images taken before the earthquake are available, including Sentinel 2, Google Earth, Gaofen 6, and Gaofen 2 images, we do not list all the satellite images taken before the 2022 Luding seismic event here.

For topographic data, we used STRM 90 m DEM for regional tectonic analysis, STRM 30 m DEM for earthquake-affected area analysis, and 12.5 m TanDEM-X for detailed landslide analysis; all SRTM topographic data were from the Geospatial Data Cloud (<http://www.gscloud.cn/>), and the TanDEM-X topographic data were from Natural Earth (<http://www.naturalearthdata.com/downloads/>). The slope was directly derived from the 12.5 m DEM on the GIS platform.

For seismic data, we used seismic intensity data (https://www.mem.gov.cn/xw/yjglbgzdt/202209/t20220911_422190.shtml) and seismogenic fault and aftershock inventories. For geological data, we used fault block data from the Qinghai-Tibet Plateau (Deng et al. 2014), the regional active fault dataset (Deng et al. 2014), regional GPS data (Zhao et al., 2015), and stratum data (1:500,000). For physical geographic data, we collected average annual rainfall (duration 2007-2018; Brocca et al. 2019), land cover (GlobeLand30: <http://www.globallandcover.com>), river and road (<https://www.webmap.cn/>) data.

For field data, one day after the mainshock, we carried out a field investigation (Fig. 4). During the field investigation, we preliminarily mapped the typical characteristics of coseismic landslides, found evidence of the relationships between tectonics and geohazards, and confirmed the coseismic landslide mapping area. As the field investigation occurred earlier than the landslide mapping, the field investigation enhanced the later landslide mapping accuracy, as numerous coseismic landslides were investigated during the field survey.

Additionally, to make a comparison with other

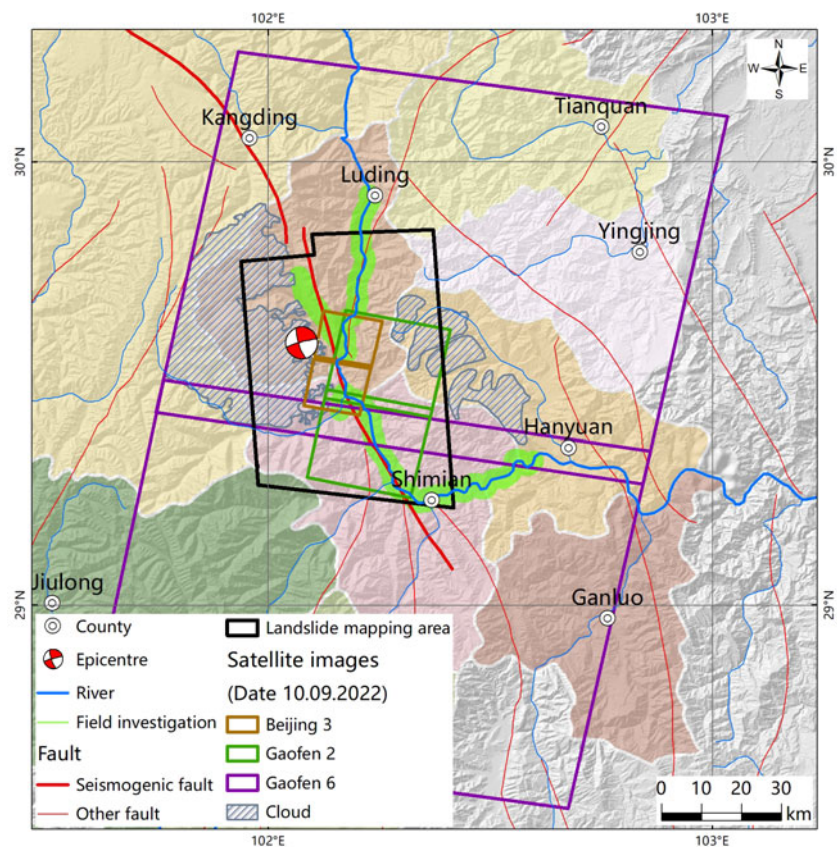


Fig. 4 Satellite image coverage and field investigation route. The areas in different colors indicate different areas of counties.

coseismic landslide inventories, we also considered the landslide inventories of the 2008 Wenchuan (Xu et al. 2014a), 2013 Lushan (Xu et al. 2015), 2017 Jiuzhaigou (Tian et al. 2019; Zhao et al. 2018), and 2022 Lushan (Zhao et al. 2022b) earthquakes. We also collected some earthquake information from other areas of the world (Xu et al. 2014a, 2015; Macro 2016; Macro et al. 2017; Fan et al. 2018; Zhao et al. 2021b, 2022b).

3.2 Landslide mapping

Before landslide mapping, we combined multiple satellite images (Gaofen 6) and field data to confirm the coseismic landslide mapping area with an area of 2,600 km² (black box in Fig. 4). We used visual interpretation to map landslides; we first imported pre- and postearthquake satellite images into the GIS platform, and then we created a polygon file to map the whole landslide boundary. Additionally, we added a point file to define the location of source area of every landslide. During landslide mapping, we also recognized landslide damming points. Finally, we

established a coseismic landslide inventory (polygon inventory and point inventory) and landslide damming inventory.

3.3 Data analysis

All data were processed on a GIS platform. Landslide density was calculated by kernel density with 1 km radius (Fig. 5B). To illustrate spatial distributions of different landslide sizes, category classification was adopted (Fig. 6A), and the spatial join operation was applied to determine the number of landslides that occurred within a specific lithologic unit, seismic intensity, rainfall, landcover, etc. Other statistical data, such as data pertaining to landslide elevations, distance to seismogenic fault and rivers, slope angle, and aspect, were also calculated on GIS platform.

To quantitatively analyze the landslide size distribution, we computed landslide number ratio (Fig. 6B), the size–frequency statistics (Fig. 6C), cumulative number ratio (Fig. 6D), relative position index r . The detail definitions of landslide number ratio, size–frequency statistics and cumulative number ratio are listed in Zhao et al (2021, 2022a).

The relative position index $r = L/S$ defines the ratio r of the distance to the valley bottom (L) to the distance between the ridge line and the valley bottom (S). The r value intervals of [0.0–0.2), [0.2–0.4), [0.4–0.6), [0.6–0.8), [0.8–1.0], and [0.9–1.0] were adopted to represent the lower, lower–middle, middle, upper–middle, and upper part and peak, respectively, of a hill (Zhao et al. 2021).

Additionally, based on other coseismic landslides on the eastern margin of the Haryan Har block, we systematically compare our findings with the results of other earthquakes, including spatial and size distribution with response to different seismogenic faults, landslide damming, etc.

4 Results

4.1 Basic characteristics

4.1.1 Spatial distribution

The inventory of coseismic landslides triggered by the 2022 Luding earthquake contains at least 4528 landslides in an area of approximately 2000 km² (Fig. 5A), and the highest landslide density reached 63

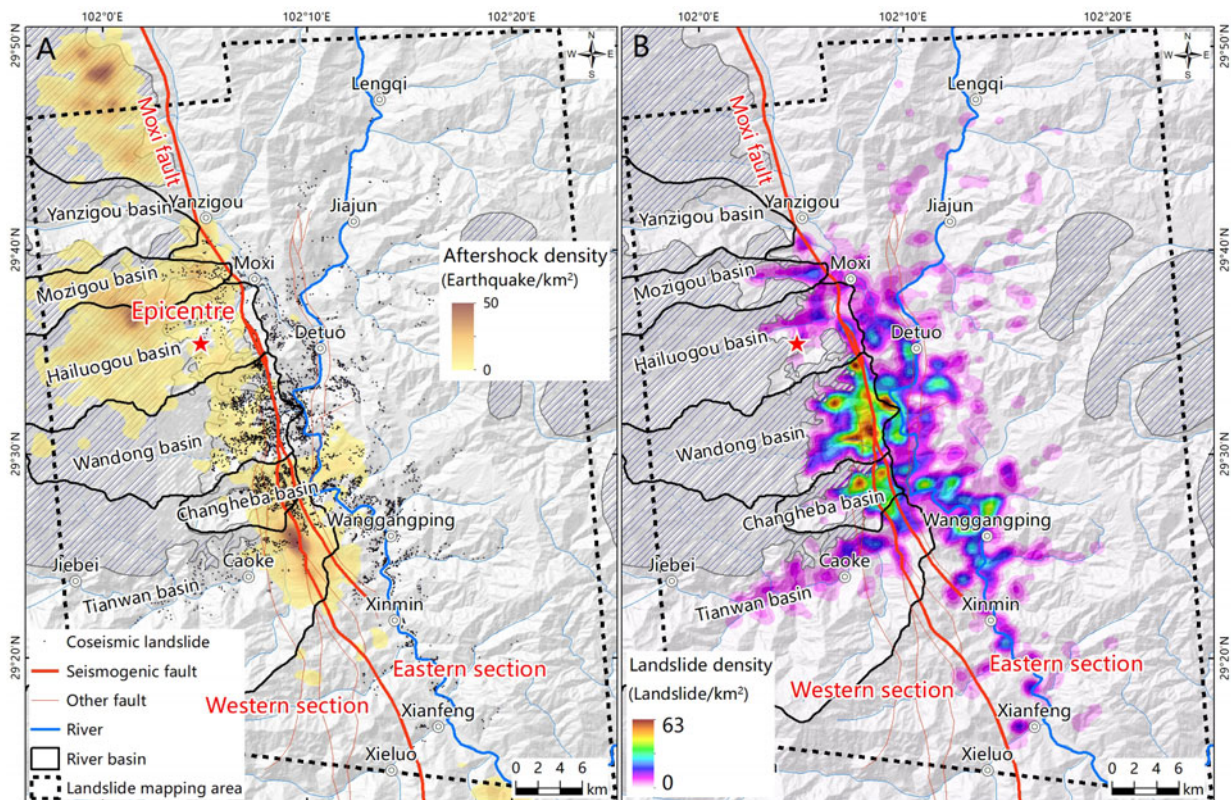


Fig. 5 Spatial distributions of coseismic landslides. (A) Size distribution, (B) density distribution.

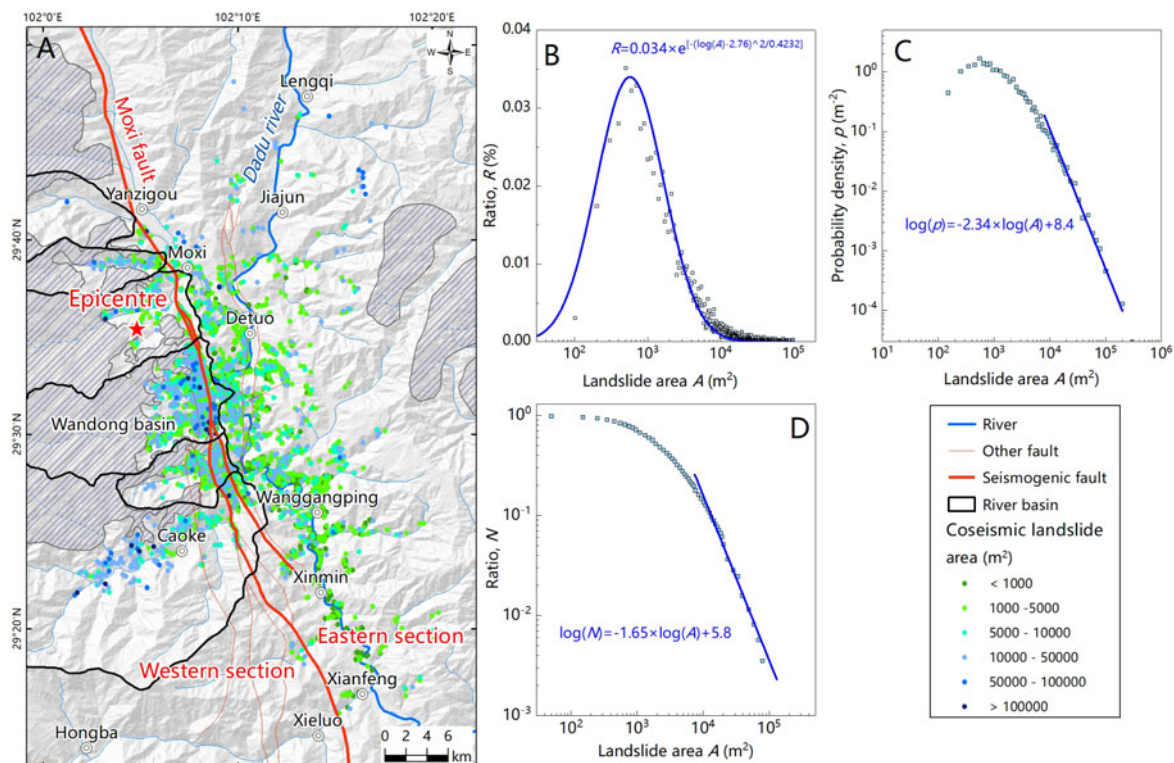


Fig. 6 Size distribution and statistical relationships of coseismic landslides. (A) Size distribution, (B) landslide number ratio vs. landslide area, (B) frequency density p vs. landslide area, (C) cumulative number ratio N vs. landslide area.

landslides/km² (Fig. 5B). The coseismic landslides are mainly concentrated in the Xinmin-Moxi section of the Dadu River, and there are no obvious landslide concentrations near the epicenter (Fig. 5). According to the corresponding seismogenic fault, the landslide area can be divided into an eastern section and a western section (Fig. 5).

The area near the seismogenic fault (Moxi fault) could be a typical area prone to coseismic landslides, as the highest concentration of landslides is distributed along it (within 2 km). The seismogenic fault usually corresponds to the strongest seismic shaking area, and this phenomenon has been observed in many seismic events worldwide (Keefer 1984, 2002; Xu et al. 2014a; Kargel et al. 2016; Fan et al. 2018; Valagussa et al. 2019).

The western section shows a higher landslide concentration (generally > 40 landslides/km²) of landslides than the eastern section (generally < 30 landslides/km², except for some small areas near the seismogenic fault; Fig. 5B). This distribution is similar to the distribution of aftershocks (Fig. 5A). According to the fault movement, the western section corresponds to the hanging wall and to the active area. This area usually exhibits stronger seismic shaking

than the footwall and passive area (Abrahamson and Somerville 1996; Chang et al. 2004; Yuan et al. 2013; Guo et al. 2013). A similar phenomenon was also observed in the 2017 Jiuzhaigou earthquake (Ling et al. 2021). However, as massive clouds still covered the western section during landslide mapping, there were only 1990 landslides identified in the western section and 2538 landslides identified in the eastern section.

Some subbasins also show high landslide concentrations, and there are 1164, 508, 380 and 187 landslides in the Wandong, Changheba, Tianwan and Hailuogou basins, corresponding to 27.3%, 11.9%, 8.9% and 4.4% of all events, respectively. All of the areas with the highest concentrations are distributed in the Wandong Basin. The Wandong, Changheba, Tianwan and Hailuogou basins are located in the western section, and the seismogenic fault crosses them (Fig. 5). Additionally, in the eastern section, the Dadu River valley has the highest concentration of coseismic landslides in its branches (Fig. 5B).

4.1.2 Size distribution

All 4528 landslides span a total area of 28.1 km², with the largest individual landslide with an area of 3.2×10⁵ m². The mean landslide area is 6211 m², and

there are 3380, 1308, 670, 68 and 17 landslides with areas larger than $1 \times 10^3 \text{ m}^2$, $5 \times 10^3 \text{ m}^2$, $1 \times 10^4 \text{ m}^2$, $5 \times 10^4 \text{ m}^2$ and $1 \times 10^5 \text{ m}^2$, respectively. Most relatively large landslides are distributed in the western section (Fig. 6A); for example, in the western section, there are 1596, 723, 407, 45, and 13 landslides with areas larger than $1 \times 10^3 \text{ m}^2$, $5 \times 10^3 \text{ m}^2$, $1 \times 10^4 \text{ m}^2$, $5 \times 10^4 \text{ m}^2$ and $1 \times 10^5 \text{ m}^2$, respectively, accounting for 47.2%, 55.3%, 61.0%, 66.2% and 76.5% of the total number of same area intervals. Landslides along the Dadu River valley are mainly small landslides with areas less than 3000 m^2 .

To quantitatively analyze the landslide size distribution, we computed the interval number ratio R (Fig. 6B), the size–frequency statistic p (Fig. 6C), and the cumulative number ratio N (Fig. 6D). The interval number ratio refers to the ratio of the number of landslides in an area intervals to the total number of landslides (Zhao et al. 2021b), and the Luding event follows an exponential distribution for areas less than 10^5 m^2 :

$$R = 0.034 \times e^{[-(\text{Log}(A)-2.76)^2/0.4332]} \quad (1)$$

where R is the interval ratio and A is the area interval value. The size–frequency statistic p is defined as $p = dN/dA$ (the ratio p between the number of landslides dN within the corresponding landslide area interval dA ; Roback et al. 2018; Tebbens 2020), and its distribution usually exhibits a power-law scaling when landslide sizes exceed a certain threshold (Tanyas et al. 2019; Tebbens 2020). The p of the Luding event is listed in Fig. 6C, and the landslides with area $> 10^4 \text{ m}^2$ exhibit a logarithmic function as follows:

$$\text{Log}(p) = -2.34 \times \text{Log}(A) + 8.4 \quad (2)$$

where p is the probability density and A is the landslide area. The cumulative number ratio N defines the cumulative number ratio N in different landslide area intervals, and its distribution also exhibits a power-law scaling when landslide sizes exceed a certain threshold (Xu et al. 2014c; Zhao et al. 2021b). The cumulative number ratio distribution of the Luding event is shown in Fig. 6D, and the landslide areas with sizes between 10^4 and 10^5 m^2 follow a logarithmic function as follows:

$$\log(N) = -1.65 \times \log(A) + 5.8 \quad (3)$$

where A is the landslide area and N is the number of landslides with a landslide area larger than A . In addition to the landslide area, the landslide volume could also be an important indicator of the regional

erosion rate and the activity level after debris flows. As the actual landslide volume is difficult to obtain, a classical empirical equation can help to estimate it, and the general relationship is expressed as follows (Parker et al. 2011):

$$V_L = \sum_1^n \alpha A_i^\gamma \quad (4)$$

where A_i is the landslide area, α and γ are empirical coefficients, and V_L is the estimated landslide volume. As different scholars or areas utilize different empirical coefficients, we adopted the empirical coefficients of the Wenchuan earthquake proposed by Parker et al. (2011), which are $\alpha = 0.146$ and $\gamma = 1.332 \pm 0.005$. The total coseismic landslide volume triggered by the Luding earthquake was calculated to be approximately $112.6 + 5.9 / -5.6 \text{ Mm}^3$.

4.2 Control of seismogenic structure and lithology at the macroscale

As the preliminary distribution law indicates that seismogenic fault areas belong to typical landslide-prone areas, we analyzed this phenomenon in detail (Figs. 7, 8 and 9). The satellite and field images in the meizoseismal area show that the seismogenic fault area contains many more landslides than recent nonseismogenic fault areas (Fig. 7). For example, the recent Detuo fault that extends along the Dadu River is an active fault (Wu 2013; Zhao et al. 2021c), and few landslides except for some shallow landslides or rock falls have occurred along it (Figs. 7A and 7B), while mountains near the Moxi fault host numerous landslides (Figs. 7A, 7C and 7D). Additionally, as the Moxi fault just crosses the Wandong River, two banks of the Wandong River host densely distributed landslides, while the nearby Dadu River valley hosts fewer landslides (Fig. 7A). Thus, this seismogenic fault influences the regional occurrence of coseismic landslides.

Furthermore, with increasing distance to the seismogenic fault, the number of landslides decreases (Fig. 8A), and there are 1335, 3783, and 4421 landslides distributed within 1, 5 and 10 km of the seismogenic fault, corresponding to 29.5%, 83.5% and 97.6% of the total number of landslides, respectively. Among the two sections, the western section presents a sharp decrease with increasing distance to the seismogenic fault (Fig. 8B), and there are 934 and 1847 landslides distributed within 1 and 5 km of the seismogenic fault, corresponding to 46.9% and 92.8% of the total number of landslides, respectively. The

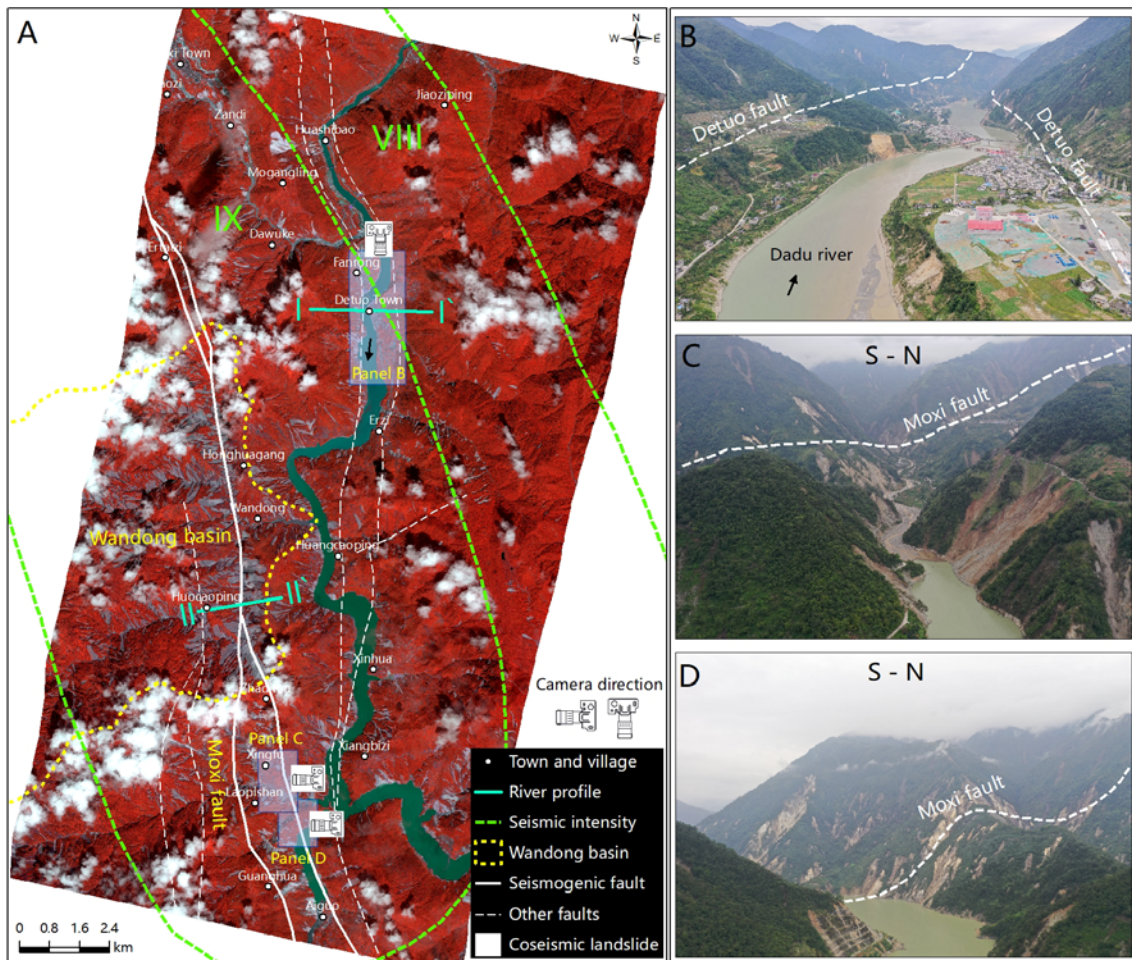


Fig. 7 Coseismic landslides concentrated along seismogenic faults. (A) The satellite image shows the spatial distribution of coseismic landslides near the seismogenic fault, and (B, C and D) the field images show obvious distribution differences between seismogenic fault (Moxi fault) and nonseismogenic faults (Detuo fault). The profiles I-I' and II-II' are shown in Figs. 11A and 11B.

eastern section presents a wavy distribution within 5 km of the seismogenic fault, and this area belongs to the Dadu River valley (Fig. 8B).

From the relationship between the distance to the seismogenic fault and elevation of the landslides, landslides in the western section are obviously generally higher than those in the eastern section, especially for the Dadu River valley, which is the area with the lowest elevations (Fig. 8C). When the distance to the seismogenic fault is over 6 km, the elevations of landslides in the western section remain similar, and those in the eastern section increases gradually (Fig. 8C). Coseismic landslides mainly occurred at intensities of VII, VIII and IX. In the study area, 3176 landslides were distributed in the area with a seismic intensity of IX, accounting for 70% of the total number of landslides (Fig. 8D). There are 1480 and 1697 landslides in the areas with a seismic

intensity of IX of the eastern and western sections, accounting for 58.3% and 85.2% of the total number of individual landslides in the eastern and western sections (Figs. 8E and 8F).

A total of 1438, 980, 855, 577 and 205 landslides occurred in T1 (early Sinian granite), T2 (early Proterozoic Heiyangbaozi superunit), T3 (Middle Triassic Leikoupo group) and T4 (Upper Triassic Zagunao group), accounting for 31.8%, 21.6%, 18.9% and 12.7% of the observed landslides, respectively (Fig. 9A). We also determined the controlling lithologies in every stratum (Fig. 9B) and found that 1479, 1060, 980 and 578 landslides occurred in R1 (granite), R2 (dolomite), R3 (quartz diorite) and R4 (quartz sandstone) rocks, accounting for 32.7%, 23.4%, 21.6% and 12.8%, respectively. Thus, the distribution of granite, dolomite and quartz could influence regional landslide occurrence. Additionally, our field survey found that landslides in

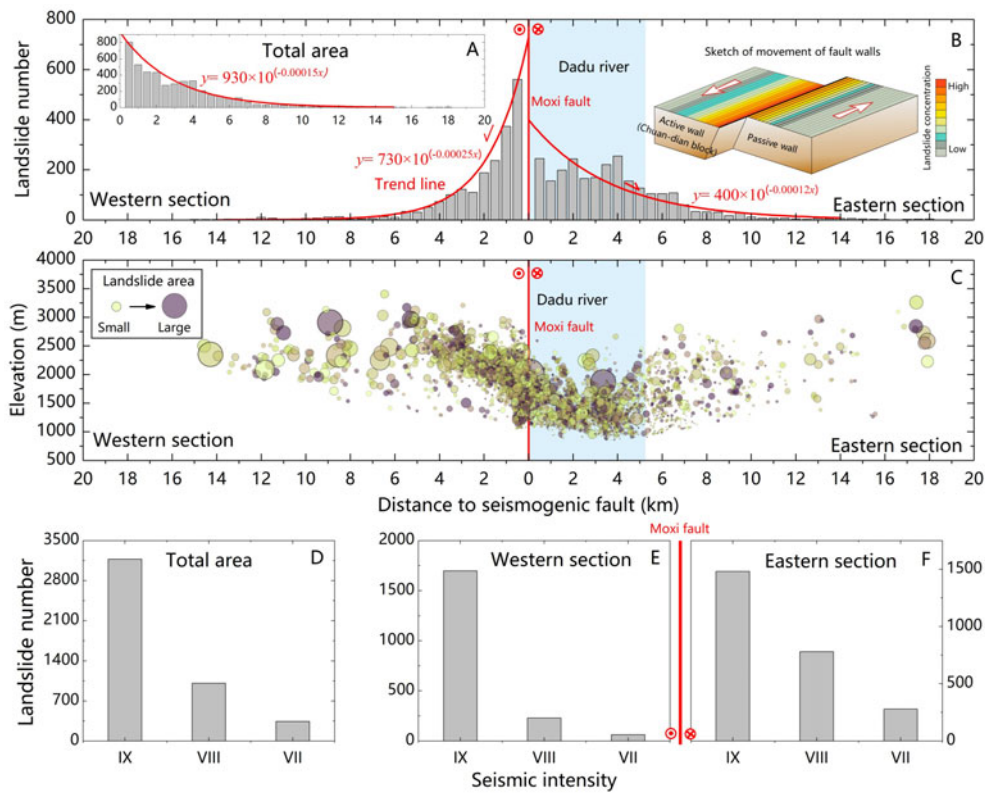


Fig. 8 Landslide distributions with respect to the seismic characteristics. (A, B and C) Seismogenic fault, (D, E and F) seismic intensity.

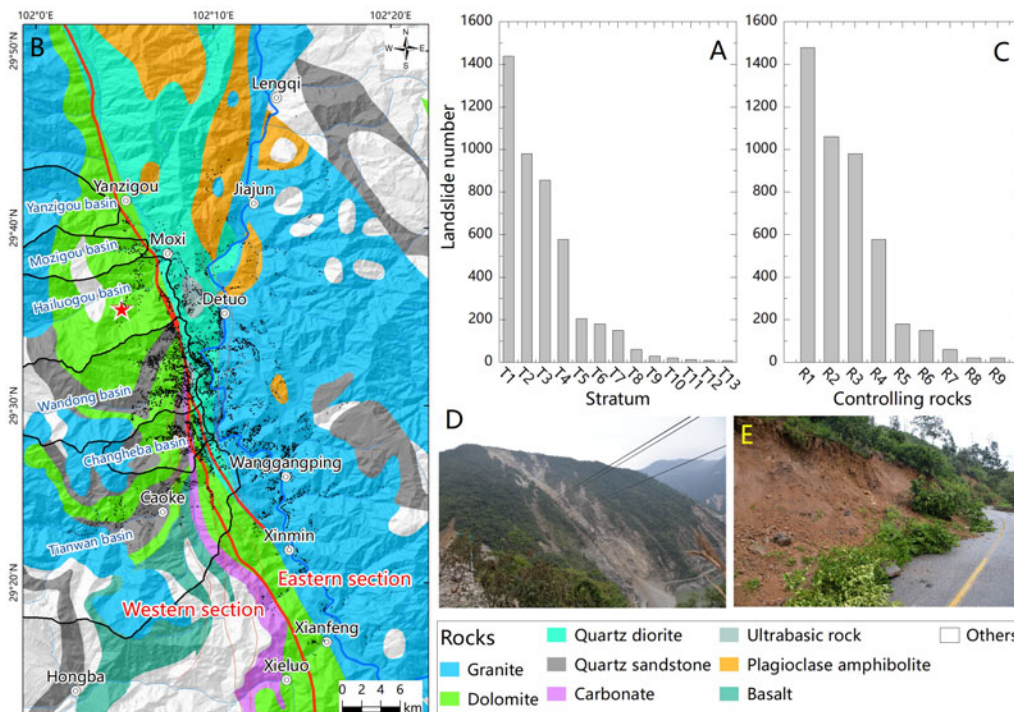


Fig. 9 Landslide distributions with respect to geological characteristics. (A) In different strata, (B and C) in different controlling lithologies, (D) higher coseismic landslides mainly occurred in rock slopes, and (E) some small landslides occurred in Quaternary slopes. In Panel A, the introductions of T1 – T13 are listed in caption of Fig. 2. In Panel B, R1 – Granite, R2 – Dolomite, R3 – Quartz diorite, R4 – Quartz sandstone, R5 – Carbonate, R6 – Ultrabasic rock, R7 – Plagioclase amphibolite, R8 – Basalt, R9 – other rocks.

middle-upper slopes or with larger areas are mainly rock landslides (Fig. 9D), and the controlling structures and lithologies could reflect their composition. While numerous soil landslides remain as surficial eluvial talus widely covering mountains (Fig. 9E), they are usually small landslides or occur along roads or river bank feet, and thick forests usually cover them. As satellite images cannot capture them very well, the current landslide inventory contains fewer soil landslides than expected. Therefore, the controlling structural and lithologic distribution could reflect the actual distribution of the current landslide inventory.

4.3 Complexity of local topography controls landslide occurrence at the microscale

As seismogenic faults and lithology control the concentration of coseismic landslides in a certain region, this chapter discusses the influence of local topography on detailed occurrence locations. Here, we adopted elevation, distance to river, relative position index r (the detail definition is listed in Section 3.2) and slope as geomorphic indicators (Fig. 10).

Regarding elevation, 1000–2200 m could be the landslide-prone area, and there are 3621 landslides concentrated in this interval, accounting for 80% of the total number (Fig. 10A). With increasing elevation,

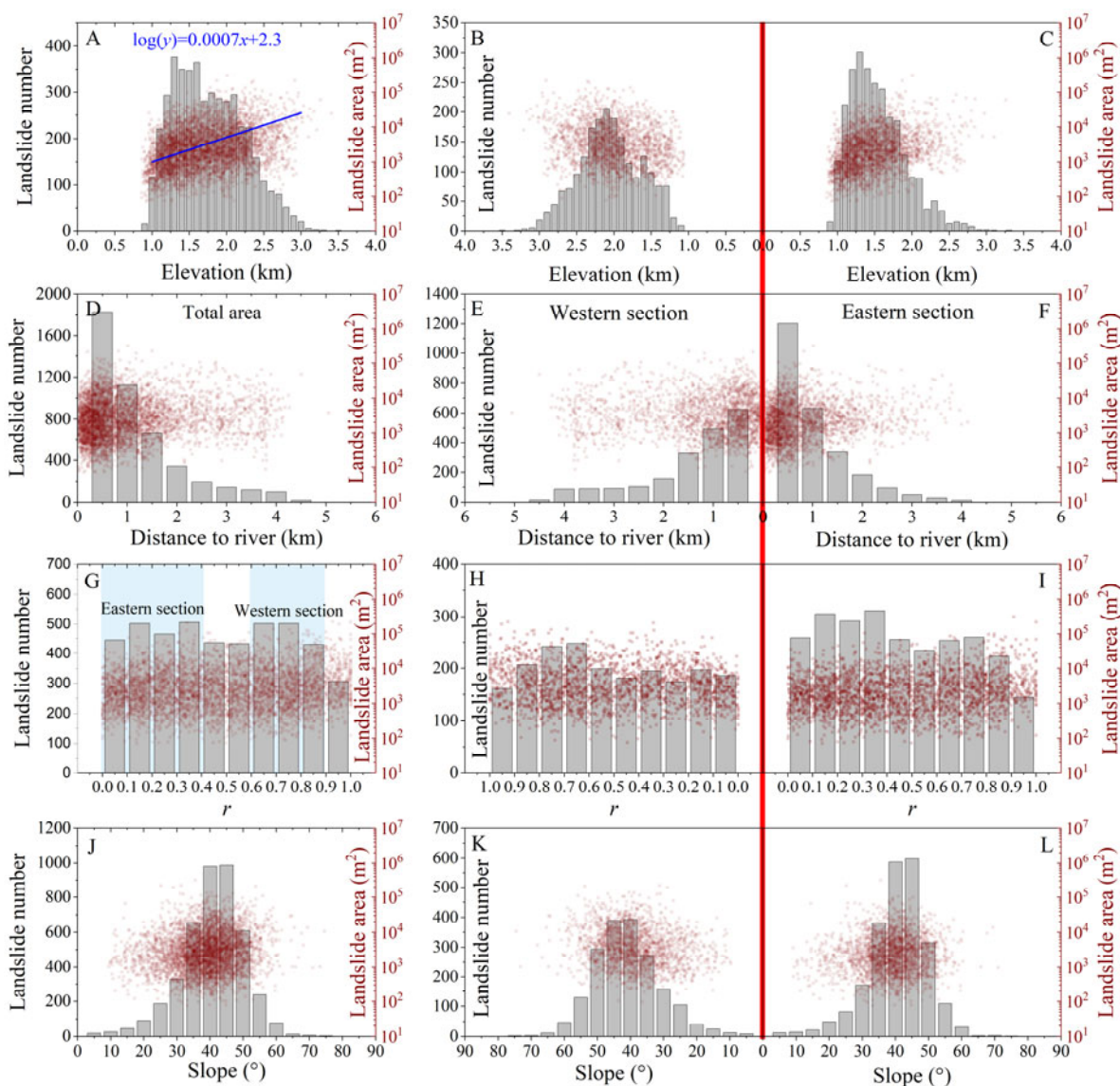


Fig. 10 (A, B and C) Elevation, (D, E, and F) distance to river, (G, H and I) relative position r and (J, K, and L) slope, and their impacts on the spatial distribution of coseismic landslides.

the landslide area increases and follows the relationship $\log(y) = 0.0007x+2.3$ (where x is the elevation and y is the landslide area). The western section has a higher controlling elevation interval (1800–22400 m, 1153 landslides, 57.9% of landslides in the western section) than the eastern section (1000–1600 m, 1738 landslides, 68.5% of landslides in the eastern section; Figs 10B and 10C). Both sections also present an increase landslide area with an increase in elevation.

For the whole study area, as the coseismic landslides show increasing distance to the river, the number of landslides decreases (Fig. 10D), and the two sections present similar phenomena (Figs. 10E and 10F). Landslides in the eastern section were influenced by rivers more obviously than those in the western section. For example, in the eastern section, there are 1203 and 2170 landslides that occurred within 500 and 1500 m of the distance to the river, accounting for 47.4% and 85.5%, respectively, while the western section has 624 and 1445 landslides, accounting for 31.4% and 72.6%, respectively. There are no obvious relationships between landslide area and distance to river.

For the relative position index r , the whole area exhibits two peaks at intervals of 0.1–0.4 (lower section of the hill) and 0.6–0.9 (upper-top section of the hill) (Fig. 10G), and the r distribution of the two

sections shows peaks at intervals of 0.1–0.4, which are mainly concentrated in the eastern section, and peaks at intervals of 0.6–0.9, which are mainly concentrated in the western section (Figs. 10H and 10I). There are no obvious relationships between the landslide area and r value. Slopes of 35°–50° are in the controlling slope intervals of all sections (Figs. 10J, 10K and 10L).

From the above, we conclude that landslides in the eastern section are prone to occur at lower elevations (1000–1600 m), lower sections of the slopes (r : 0.1–0.4), and close to the river (< 1000 m), and landslides in the western section are prone to occur at relatively high elevations (1800–2500 m) and upper-top sections of slopes (r : 0.6–0.9). We mapped these restrictions on typical river profiles of two sections (Fig. 11). We found that the landslide-prone area in the eastern section coincides with the location of the gorge section of the Dadu River valley, and the upper wide valley section is a secondary landslide-prone area (Figs. 11A and 11A1). The lower gorge section usually has more fractures than the wide valley, caused by intensive erosion, strong unloading, the steep slope, etc. (Wang et al. 2007, 2013; Bai et al. 2020). Additionally, we suspect that the bank slope foot, where roads are usually located, is also a landslide-prone area, as there exist numerous small soil landslides distributed in this area (Fig. 11A2), but

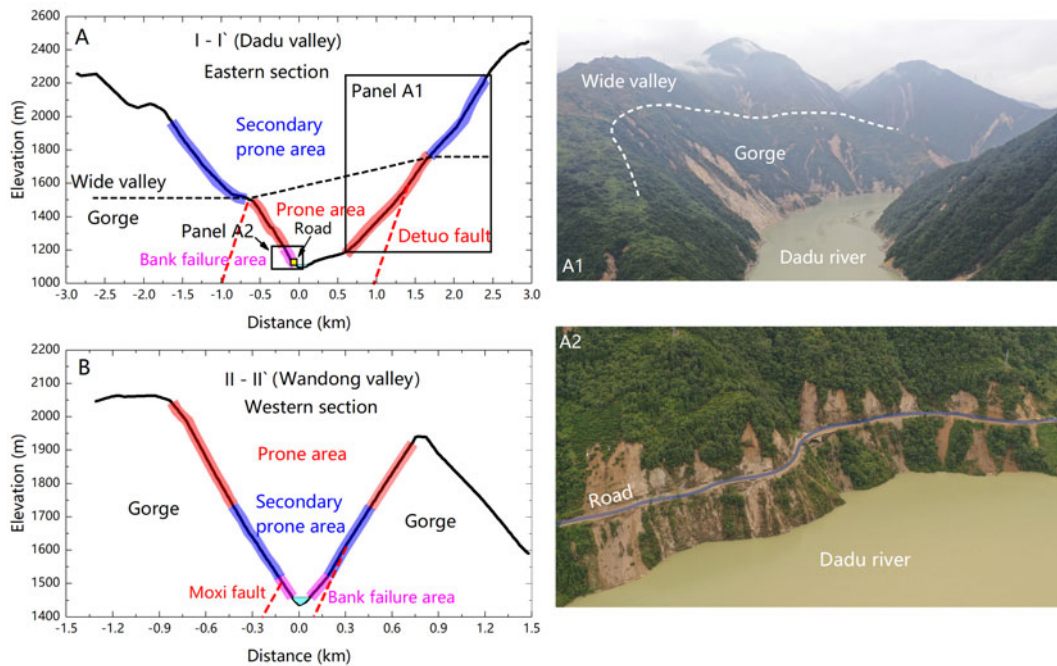


Fig. 11 Typical profile sketches of valleys in the (A) eastern section and (B) western section showing landslide-prone areas, respectively, and (A1 and A2) field images showing the landslide distribution in eastern section. The locations of profiles I-I' and II-II' are listed in Fig. 7A.

the remote images could not capture them very well because they are too small and are covered with a thick forest.

The landslide-prone area in the western section coincides with the upper-top section of the gully (Fig. 11B), and as these gullies belong to branches of the Dadu River, they characterize typical gorge landforms. Some monitoring results have revealed that the upper-top section of the gorge could provide stronger site amplification than the lower section, whose amplification factor could reach 5-12 times (Luo et al. 2014; Zhao et al. 2020a). Therefore, the upper-top section with stronger seismic shaking could have triggered more landslides. Additionally, we suspect that the bank slope foot is also a landslide-prone area (Fig. 11B).

Coseismic landslides are concentrated in areas with higher annual rainfalls (> 1200 mm/yr; Fig. 12A), especially in the interval of 1450-1550 mm/yr (3155

landslides, accounting for 69.7%; Fig. 12C). As landslide-affected areas mainly coincide with forest areas (Fig. 12B), 3800 landslides occurred in forest areas (Fig. 12D).

5 Discussion

5.1 Comparison with other earthquakes in the eastern Baryan Har block

5.1.1 Spatial distribution with respect to different seismogenic mechanisms

According to the distribution of fault blocks on the Qinghai-Tibet Plateau, the 2022 Luding event occurred on the southeastern boundary of the Baryan Har block (Fig. 13). The current Baryan Har block is very active, especially at its eastern margin. Since 2000, there have been 5 earthquakes that have caused

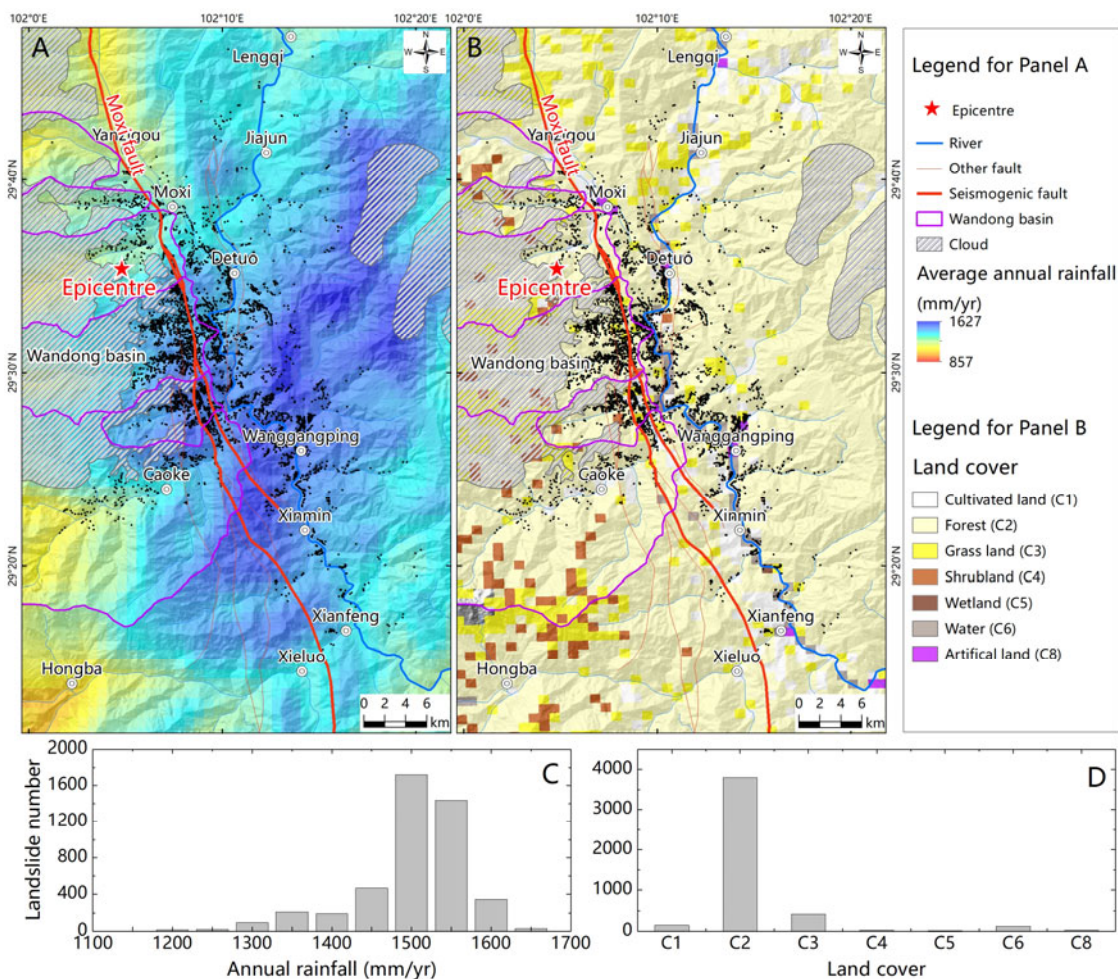


Fig. 12 Spatial distributions of landslides under different distributions of (A and C) annual rainfall and (B and D) land cover. The land cover data are from GlobeLand30 (<http://www.globallandcover.com>), and the annual rainfall data are from Brocca et al. (2019).

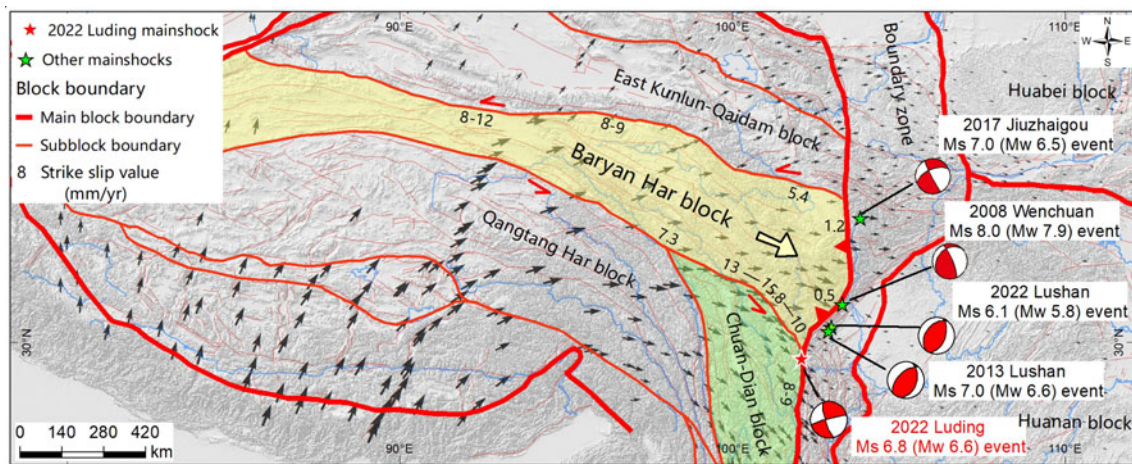


Fig. 13 Location of the Baryan Har block and the distribution of 5 large earthquakes. The block fault is from Deng et al. (2014), the GPS data is from Zhao et al. (2015).

massive landslides: the 2008 Mw 7.9 Wenchuan (197481 landslides; Xu et al. 2015), 2013 Mw 6.6 Lushan (15645 landslides; Xu et al. 2015; 3810 landslides; Tang et al. 2015), 2017 Mw 6.5 Jiuzhaigou (1883 landslides; Fan et al. 2018; 4834 landslides; Tian et al. 2019), 2022 Mw 5.8 Lushan (1288 landslides; Zhao et al. 2022b) and 2022 Luding event studied here (4528 landslides). Their spatial distributions are listed in Fig. 14.

As earthquakes occurred in different locations of the boundary, earthquakes characterize different focal mechanisms, and the earthquakes (2008 Wenchuan earthquake, 2013 and 2022 Lushan earthquakes) that occurred at the eastern boundary were caused by the Longmenshan thrust fault (Xu et al. 2009, 2013; Zhao et al. 2022b), which is a nappe structure (Chen and Wilson 1996; Jia et al. 2010). These earthquakes characterize thrust movement with slight dextral strike-slip (Xu et al. 2009). The earthquakes located on the southern boundary (the 2022 Luding earthquake and the 1786 Moxi earthquake; Dai et al. 2005; Zhao et al. 2021c) were both caused by the Xianshuihe fault with sinistral strike-slip motion (Papadimitriou et al. 2004; Ran et al. 2008, 2010; Wang et al. 2014). The earthquake located on the northern boundary (2017 Jiuzhaigou earthquake) was caused by the east Kunlun fault with sinistral strike-slip motion (Ren et al. 2017).

The coseismic landslides along the eastern boundary were triggered by thrust events, and their distributions exhibit an obvious hanging wall effect. The hanging wall hosts more landslides than the footwall (Figs. 14A, 14B, 14C, 14D, 14G, 14H, 15A), especially for the 2008 Wenchuan earthquake. The

seismic monitoring of the Wenchuan earthquake indicates that the hanging wall is characterized by stronger shaking than the footwall at the same distance to the seismogenic fault (Fig. 15B; Abrahamson and Somerville 1996; Chang et al. 2004; Guo and Hamada 2013). Additionally, the landslide-affected area in the hanging wall could extend 20-50 km (Figs. 14 and 15; Xu et al. 2014a, 2015; Zhao et al. 2020b).

Coseismic landslides at the southern and northern boundaries were triggered by seismic events with sinistral strike-slip motion, and their distributions exhibit an active area effect, i.e., the active area concentrates more landslides than the passive area, and the landslide-affected area in the active area could extend 10-20 km (Figs. 8A, 8B, 14E, 14F and 15C). The 20 km is estimated from the Luding event, as the cloud covers the area 14 km or farther from the seismogenic fault, but there should be coseismic landslides there. Although the two events are both strike-slip events, the southern boundary presents more intensive tectonic movement (strike-slip rate 10-13 mm/yr; Deng et al. 2014) than the northern boundary (strike-slip rate 5.4 mm/yr; Deng et al. 2014). This indicates that the southern boundary could accumulate more strain energy rapidly and has a higher geostress, resulting in more frequent earthquakes and more fractured rocks.

Combining the above results, we summarized the effects of fault types on landslide distribution in the eastern Baryan Har block, as shown in Fig. 15D. We consider the eastern boundary (Longmenshan fault) with thrust movement to be the primary coseismic landslide-prone area, the southern boundary (Moxi section of the Xianshuihe fault) to be the secondary

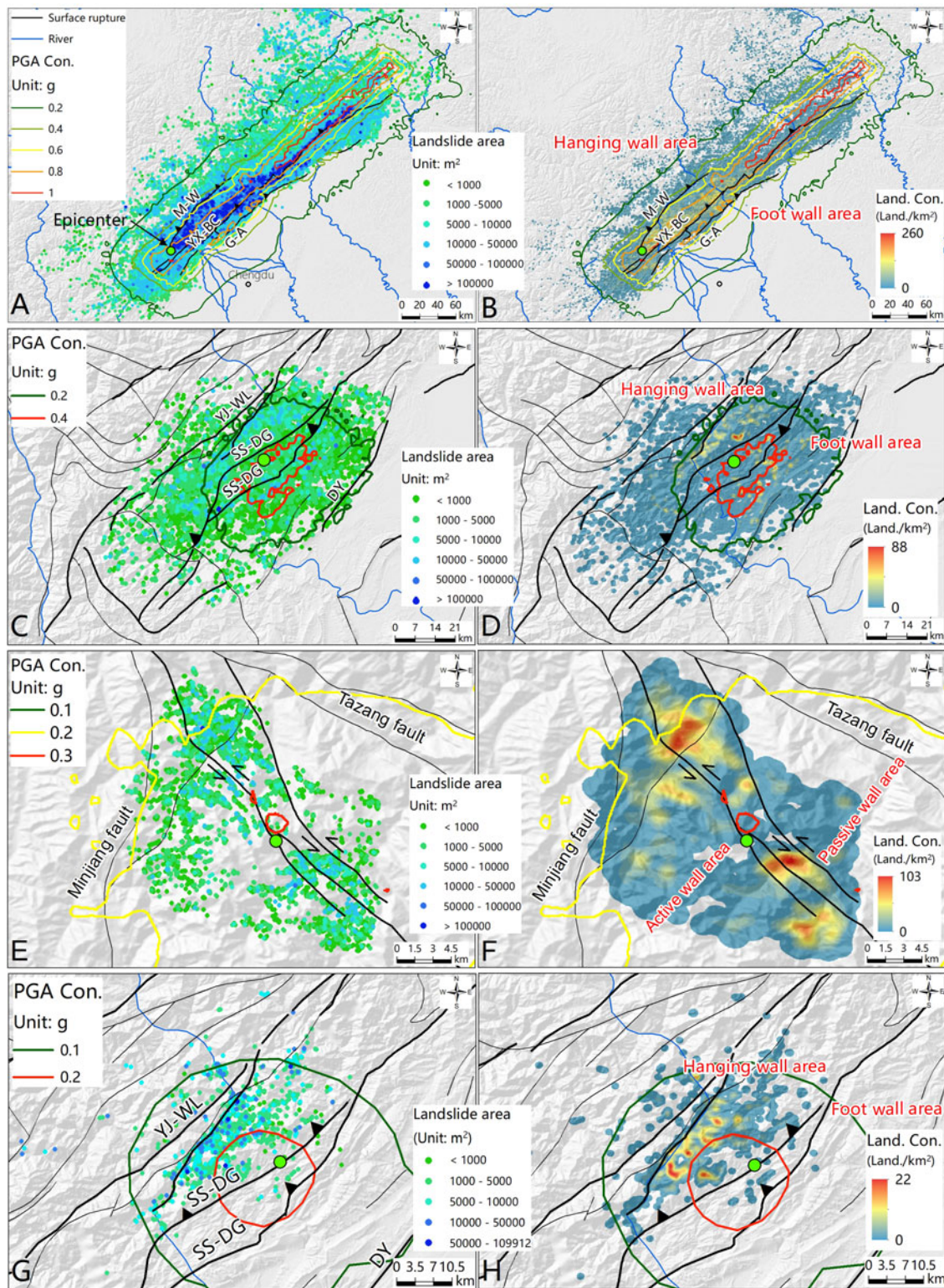


Fig. 14 Spatial and size distribution of the (A and B) 2008 Wenchuan, (C and D) 2013 Lushan, (E and F) 2017 Jiuzhaigou, and (G and H) 2022 Lushan events. Landslide inventories of 2008 Wenchuan, 2013 Lushan, 2017 Jiuzhaigou and 2022 Lushan earthquakes are from Xu et al. (2014a, 2015), Tian et al. (2019) and Zhao et al. (2022b). All PGA contours are from USGS (<https://www.usgs.gov/>). In Panels A and B, M-W – Maoxian-Wenchuan fault, YX-BC – Yingxiu-Beichuan fault, G-A – Guanxian-Anxian fault. In Panels C and G, YJ – WL – Yanjin –Wolong fault, SS-DG – Shuangshi – Dagan fault, DY – Dayi fault.

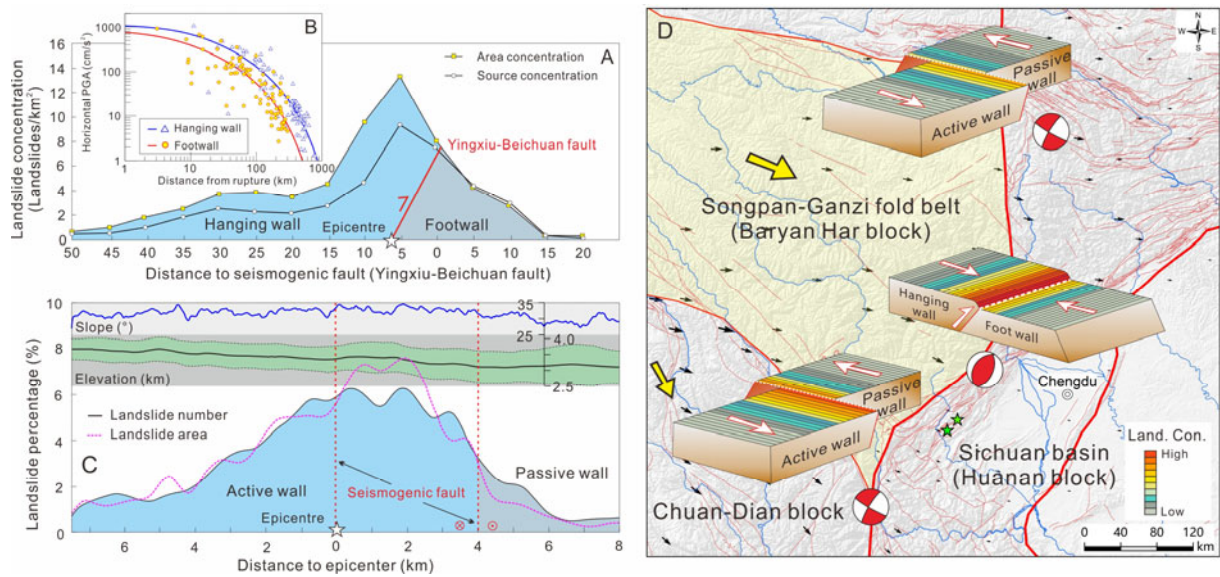


Fig. 15 Seismic characteristics influence the spatial distribution of landslides. (A and C) Relationships of landslide distribution and distance to seismogenic fault, (A) Wenchuan and (C) Jiuzhaigou earthquakes, (B) spatial distribution of PGA in hanging wall and footwall areas (Wenchuan earthquake), (D) schematic representation of effects of fault types on landslide distribution in the eastern Baryan Har block. The Panel A is derived from Yuan et al. (2013), the Panel B is derived from Guo and Hamada (2013), the Panel C is derived from Ling et al. (2021).

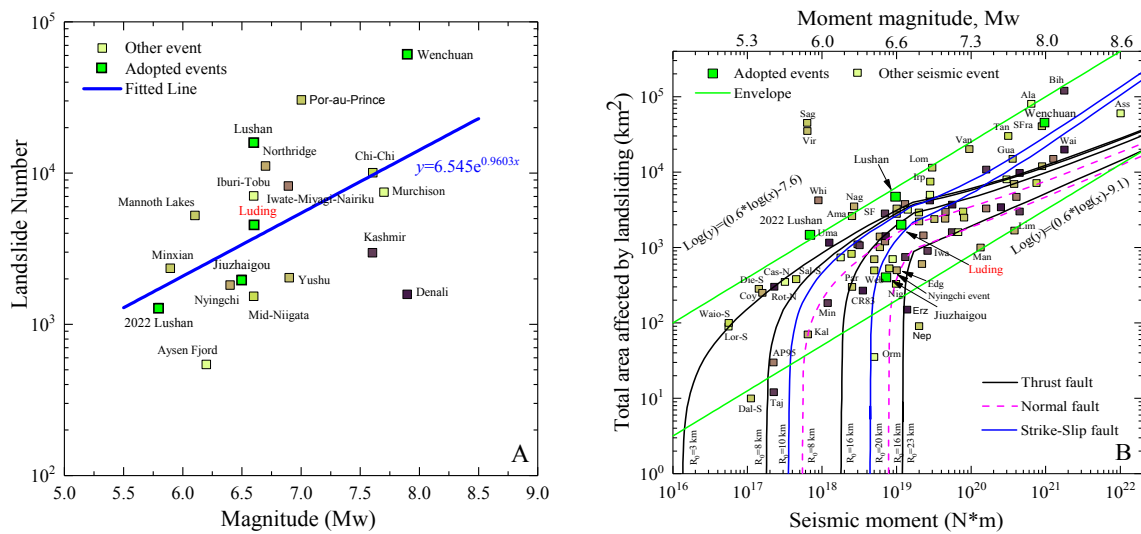


Fig. 16 Characteristics of the (A) number of landslides and (B) total affected area impacted by the Luding event compared to other seismic events worldwide. In Panel A, other events are from Fan et al. (2018), Zhao et al. (2020b, 2022b), the base map of Panel B is retrieved from Marc et al. (2017).

landslide-prone prone area, and the northern boundary (east Kunlun fault) to be the tertiary landslide-prone area.

5.1.2 Landslide sizes

To compare the landslide sizes of different earthquakes along the eastern margin, we collected landslide number, landslide area, and landslide volume data (Figs. 16, 17 and 18). For landslide number, the relationship between landslide number

(y) and seismic magnitude (x) follows an exponential distribution of $y = 6.54e^{0.9603x}$ (Fig. 16A; Fan et al. 2018; Zhao et al. 2021b), and the Wenchuan, Lushan, and Luding earthquakes lie above the fitting line; the Jiuzhaigou and 2022 Lushan earthquakes lie below the fitting line (Fig. 16A). Regarding the landslide-affected areas, all earthquakes are distributed within the two envelopes of $\log(y) = 0.6 \cdot \log(x) - 7.6$ (upper envelope) and $\log(y) = 0.6 \cdot \log(x) - 9.1$ (lower envelope), where y is the landslide-affected area (km^2)

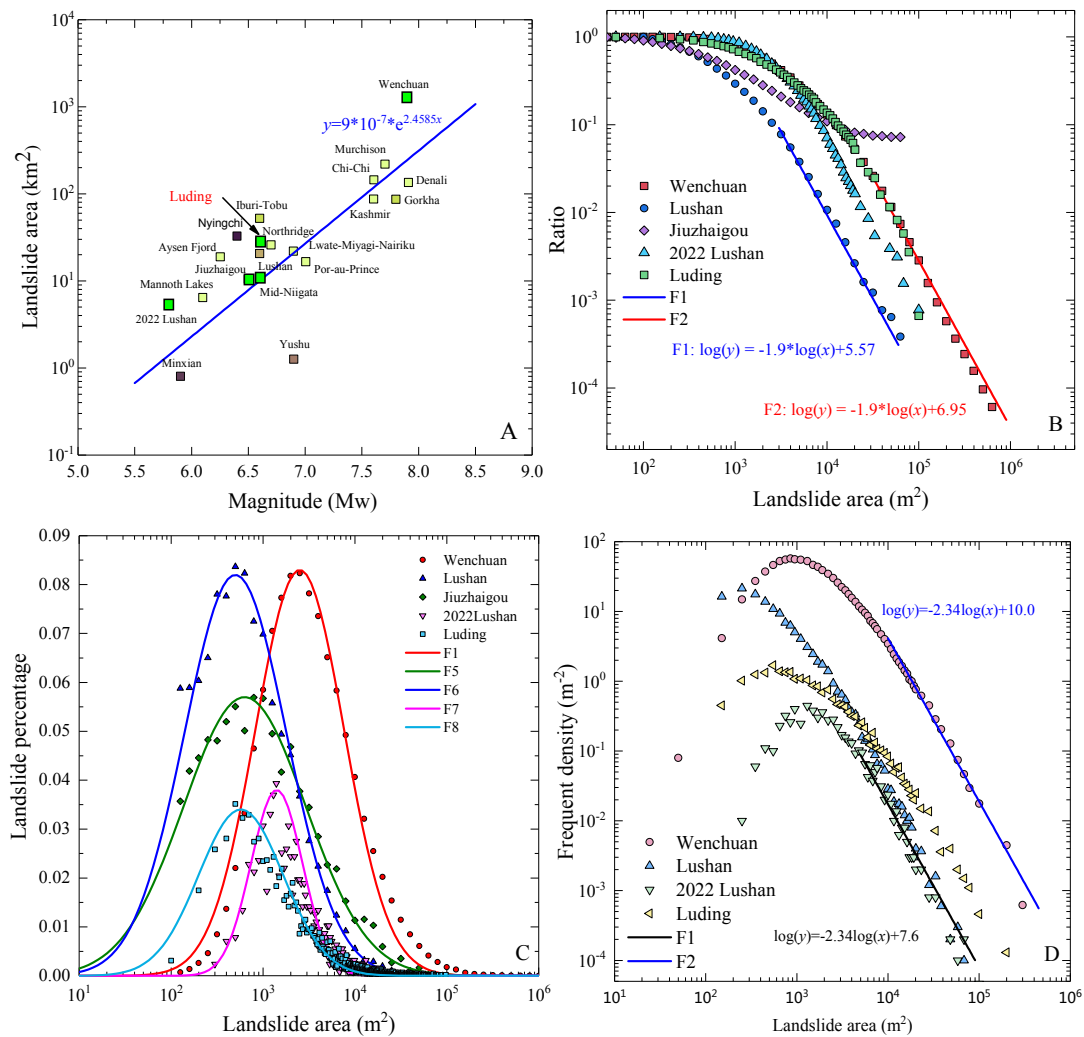


Fig. 17 Characteristics of different coseismic landslide areas on the eastern margin of the Baryan Har block. (A) Total area distribution (the other events are obtained from Xu et al. (2014a, 2015); Fan et al. (2018), and Zhao et al. (2021b, 2022b)). (B) Relationship between the cumulative number of landslides N and the landslide area (the other events are based on Xu et al. (2015) and Zhao et al. (2022b)). (C) Landslide number ratios in the different landslide area intervals (the other events are retrieved from Xu et al (2014a) and Zhao et al (2022b)). (D) Landslide area versus the frequency density relationship (the other events are based on Fan et al. (2018) and Zhao et al. (2022b)).

and x is the seismic magnitude (Fig. 16B). The Luding earthquake lies between the Lushan (upper) and Jiuzhaigou (lower) earthquakes.

For the total landslide areas, all earthquakes are located above the trending line, and the total area of the Luding earthquake is higher than that of the Lushan and Jiuzhaigou earthquakes (Fig. 17A). For the cumulative number of landslides N , except for the Jiuzhaigou earthquake, the other earthquakes follow similar distributions and lie between two trend lines (F1: $\log(y) = -1.9 \cdot \log(x) + 5.57$, F2: $\log(y) = -1.9 \cdot \log(x) + 6.95$), and the Luding earthquake has a similar distribution to the Wenchuan earthquake (Fig. 17B). All interval number ratio distributions follow normal distributions but have different coefficients

(Fig. 17C). The frequency density distributions follow similar trends and lie between two trend lines (F2: $\log(y) = -2.34 \cdot \log(x) + 7.6$, F2: $\log(y) = -2.34 \cdot \log(x) + 10.0$), and the Luding earthquake lies between two trend lines but closer to the lower trend line (Fig. 17D). Regarding the landslide volumes, the Lushan, Jiuzhaigou and Luding earthquakes are all located higher than the range of other events and fitting lines of Keefer (1994) and Marc (2016), and the Luding event has the largest total volume among these three events (Fig. 18).

5.1.3 Landslide damming

According to satellite images (satellite image date: 10 September 2022), we also mapped landslide

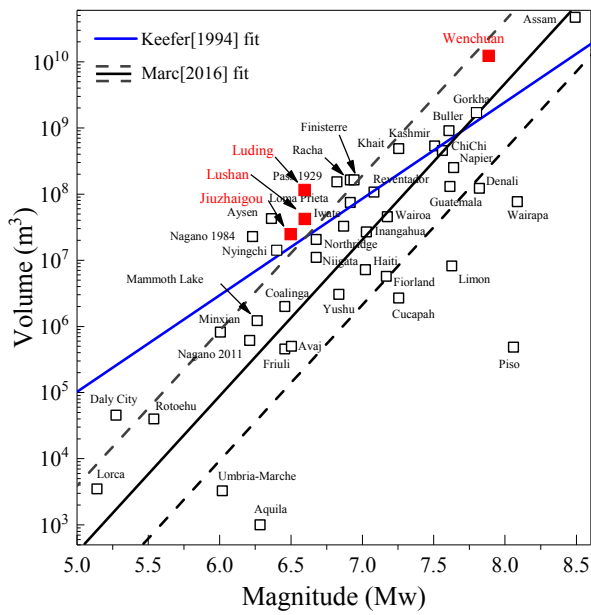


Fig. 18 Characteristics of estimated total landslide volumes. Other data are from Marc (2016) and Zhao et al. (2021b).

damming, and we divided the dams into full blockage (with a dammed lake) and partial blockage (without a dammed lake) (Xu et al. 2009; Fan et al. 2012). There were at least 30 landslide damming points triggered by the Luding earthquake; 16 cases were full blockages, and the other 14 cases were partial blockages (Fig. 19A). Seventeen dams were distributed along seismogenic faults (Fig. 19). Among the 30 dams, 21 were located in the Wandong Basin (Fig. 19B), accounting for 70% of the total number. Among 16 dammed lakes, the maximum, minimum and mean lake areas were 9472, 212 and 3005 m², respectively. For other earthquakes on the eastern margin, the Wenchuan earthquake caused 828 dams to form, 574 cases were full blockages, and 254 other cases were partial blockages (Fig. 20). Similar to the Luding earthquake, the seismogenic fault area also belongs to the landslide dam prone area (Fig. 20).

5.2 Limitations

Combined with field investigation and remote sensing interpretation, this study attempts to analyze the influence of geomorphic and tectonic indexes on landslide occurrence. However, there remain some limitations in landslide mapping and relative analyses.

With regard to the landslide mapping, as mentioned in Sections 4.1 and 4.2, clouds widely covered the earthquake-affected area during imaging,

especially in the high mountain area (elevation > 2500 m) of the western section, and this area also belongs to the potential landslide-prone area. Unfortunately, we lack landslide data in this area, which could make the currently estimated landslide-affected area slightly smaller than the actual conditions (especially for the western section). Additionally, the field investigation found that numerous small landslides occurred along the bank slope foot (where roads and usually located), while the remote image interpretation could not recognize them very well because they are too small and have thick forest growing on them. The above limitations could cause the number of current landslides to be slightly less than the actual conditions. Although the current landslide inventory is slightly underestimated, the current data cover the whole meizoseismic region of the Luding earthquake, and the above limitations will not change the results.

Moreover, the peak ground acceleration (PGA), as an important influence index, is usually adopted to freely analyze its influence on landslide occurrence (Gorum et al. 2011; Xu et al. 2014a, 2015; Fan et al. 2018; Zhao 2021; Zhao et al. 2012a, 2021b, 2022b), and this data can be downloaded from the USGS (<https://earthquake.usgs.gov/earthquakes/map>). However, the epicenter of the Luding earthquake monitored by the USGS deviates from our field conditions, similar to the PGA data; thus, we do not adopt it in this study. Additionally, valley morphological features are closely influenced by the integrity of the rock mass, and further analysis of the relationship between the valley morphology and landslide distribution is needed.

6 Conclusions

To gain insight into the roles of geomorphic and tectonic indexes on the landslide distribution caused by the 2022 Ms 6.8 (Mw 6.6) Luding earthquake, Sichuan Province, China, we carried out field investigation and landslide mapping systematically, and established a coseismic landslide inventory using a series of high-resolution satellite images. Some conclusions could be summarized as follows.

The 2022 Luding earthquake triggered at least 4528 landslides spanning a total area of 28.1 km², and the active area is characterized by a higher landslide concentration, especially in the Wandong Basin. We

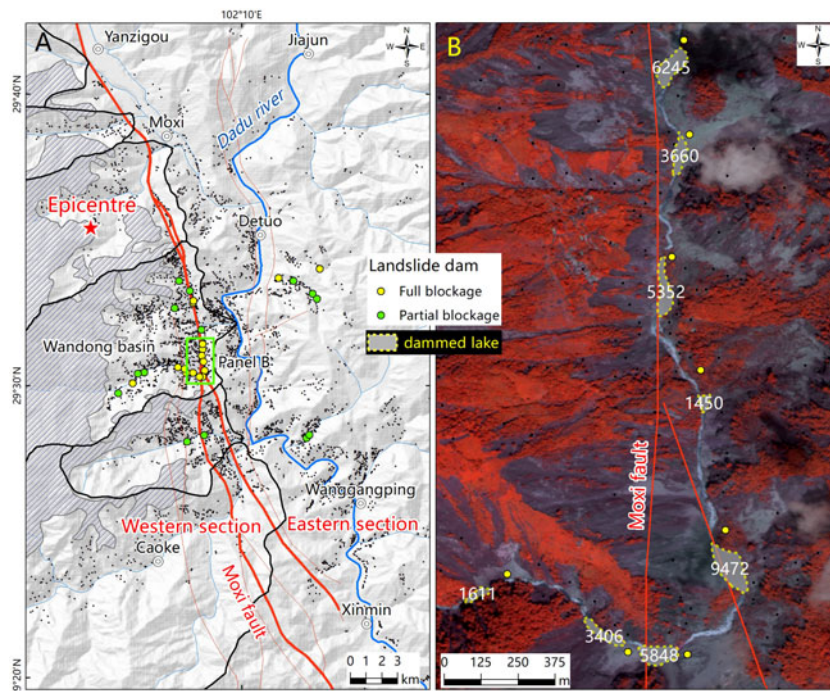


Fig. 19 Spatial distribution of landslide damming points (A) and satellite image showing some typical landslide damming points (B). The satellite image of Panel B is Beijing 3 taken on 10 September 2022.

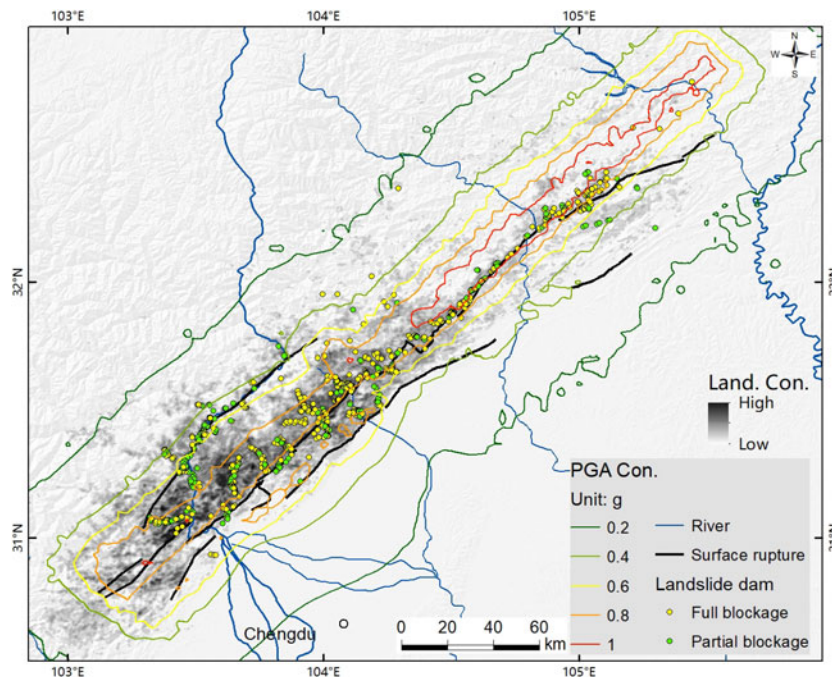


Fig. 20 Spatial distribution of landslide damming points induced by the Wenchuan earthquake. The landslide damming dataset is from Fan et al. (2012). Land. Con. – Landslide concentration, PGA Con. – PGA contour.

also find that tectonism and topography fundamentally control the spatial distribution of these landslides at different scales, as the seismogenic fault structure and lithology influence the regional distribution (more landslides closer to the seismogenic fault and some controlling lithologies),

and local topography influences the occurrence position on slopes (eastern section is prone to form landslides in the lower gorge section, and western section is prone to form landslides in the upper-top section).

The earthquakes at the eastern boundary are

caused by the Longmenshan thrust fault, characterized by thrust movement with slight dextral strike-slip motion; the earthquakes at the southern and northern boundaries were caused by the Moxi fault (southern segment of the Xianshuihe fault) and east Kunlun fault, respectively, and both are characterized by sinistral strike-slip movement, but the Moxi fault has exhibited more intensive strike-slip movement. The eastern, southern and northern boundaries could be the primary, secondary and tertiary coseismic landslide-prone areas, respectively.

Additionally, the current landslide inventory is a slight underestimation, but this has limited influences on the results. The relationship between valley morphology and landslide distribution requires further analysis.

Acknowledgements

This study was supported by National Natural Science Foundation of China (Grant No. U22A20603, U21A2008, 42007273), the Special Assistant

Researcher Foundation of Chinese Academy of Sciences (Zhao Bo), the China Postdoctoral Science Foundation (2020M673292, and 2021T140650) and the IMHE Youth S&T Foundation (SDS-QN-2106). The authors express their gratitude for this financial assistance.

The authors also thank YONG You, GE Yong-gang, OUYANG Chao-jun, NIE Yong, SU Feng-huan, FAN Jian-rong, CHEN Rong, SU Zhi-man, ZHANG Jian-qiang, MENG Qing-kai, LI Shuai, WANG Jiao, CHEN Jian-gang, JIANG Yuan-jun, ZENG Lu, HU Gui-sheng, LIU Shuang, CHANG Rui-ying from Institute of Mountain Hazards and Environment, CAS for providing remote sensing images, emergency interpretation, and other supporting; thank WANG Shi-yuan from Sichuan earthquake Administration for providing aftershock inventory; thank Prof. WANG Yun-sheng and Prof. LI Wei-le from Chengdu University of Technology for useful discussion. We also thank Editor-in-chief QIU Dunlian and Editorial Office of JMS for providing rapid handling; thank anonymous reviewers for their constructive comments.

References

- Abrahamson NA., Somerville PG (1996) Effects of the hanging wall and footwall on ground motions recorded during the Northridge earthquake. *B Seismol Soc Am* 86(1B): S93-S99. <https://doi.org/10.1785/BSSAO8601BoS93>
- Bai M, Chevalier ML, Leloup PH, et al. (2021) Spatial slip rate distribution along the SE Xianshuihe fault, eastern Tibet, and earthquake hazard assessment. *Tectonics* 40(11): e2021TC006985. <https://doi.org/10.1029/2021TC006985>
- Bai MK, Chevalier ML, Li HB, et al. (2022) Late Quaternary slip rate and earthquake hazard along the Qianning segment, Xianshuihe fault. *Acta Geol Sin* 96(7): 2312-2332. <https://doi.org/10.19762/j.cnki.dizhixuebao.2022144>
- Bai YJ, Wang YS, Ge H, et al. (2020) Slope structures and formation of rock-soil aggregate landslides in deeply incised valleys. *J Mt Sci* 17(2): 316-328. <https://doi.org/10.1007/s11629-019-5623-4>
- Brocca L, Filippucci P, Hahn S, et al. (2019) SM2RAIN-ASCAT (2007-2018): global daily satellite rainfall data from ASCAT soil moisture observations. *Earth Syst Sci Data* 11: 1583-1601. <https://doi.org/10.5194/essd-11-1583-2019>
- CCTV (2022) The Luding earthquake had caused 93 casualties. <http://news.cctv.com/2022/09/12/ARTIAMl4krq39vCR9fwbmJ9f220912.shtml>
- Chang TY, Cotton F, Tsai YB, et al. (2004) Quantification of hanging-wall effects on ground motion: some insights from the 1999 Chi-Chi earthquake. *B Seismol Soc Am* 94(6): 2186-2197. <https://doi.org/10.1785/0120030233>
- Chen GH, Xu XW, Wen XZ, et al. (2016) Late Quaternary slip rates and slip partitioning on the southeastern Xianshuihe fault system, eastern Tibetan Plateau. *Acta Geol Sin* 90(2): 537-554. <https://doi.org/10.1111/1755-6724.12689>
- Chen H, Lin GW, Lu MH, et al. (2011) Effects of topography, lithology, rainfall and earthquake on landslide and sediment discharge in mountain catchments of southeastern Taiwan. *Geomorphology* 133(3-4): 132-142. <https://doi.org/10.1016/j.geomorph.2010.12.031>
- Chen SF, Wilson CJ (1996) Emplacement of the Longmen Shan Thrust-Nappe Belt along the eastern margin of the Tibetan Plateau. *J Struct Geol* 18(4): 413-430. [https://doi.org/10.1016/0191-8141\(95\)00096-V](https://doi.org/10.1016/0191-8141(95)00096-V)
- Chen XL, Ran HL, Yang WT (2012) Evaluation of factors controlling large earthquake-induced landslides by the Wenchuan earthquake. *Nat Hazard Earth Sys* 12(12): 3645-3657. <https://doi.org/10.5194/nhess-12-3645-2012>
- Clarke BA, Burbank DW (2010) Bedrock fracturing, threshold hillslopes, and limits to the magnitude of bedrock landslides. *Earth Planet Sci Lett* 297(3-4): 577-586. <https://doi.org/10.1016/j.epsl.2010.07.011>
- CENC (2022) 2022.09.05 Luding Ms 6.8 Earthquake, Sichuan Province, China. <https://news.ceic.ac.cn/CC20220905125218.html>
- Conforti, M., Ietto, F. 2020. Influence of tectonics and morphometric features on the landslide distribution: a case study from the Mesima Basin (Calabria, South Italy). *J. Earth Sci.* 31(2), 393-409. <https://doi.org/10.1007/s12583-019-1231-z>
- Dai FC, Lee CF, Deng JH, et al. (2005) The 1786 earthquake-triggered landslide dam and subsequent dam-break flood on the Dadu River, southwestern China. *Geomorphology* 65(3-4): 205-221. <https://doi.org/10.1016/j.geomorph.2004.08.011>
- Deng QD, Cheng J, Ma J, et al. (2014) Seismic activities and earthquake potential in the Tibetan Plateau. *Chinese J Geophys* 57(5): 678-697. <https://doi.org/10.1002/cjg2.20133>
- Fan X, Scaringi G, Korup O, et al. (2019) Earthquake - induced

- chains of geologic hazards: Patterns, mechanisms, and impacts. *Rev Geophys* 57(2): 421-503.
<https://doi.org/10.1029/2018RG000626>
- Fan X, Scaringi G, Xu Q, et al. (2018) Coseismic landslides triggered by the 8th August 2017 Ms 7.0 Jiuzhaigou earthquake (Sichuan, China): factors controlling their spatial distribution and implications for the seismogenic blind fault identification. *Landslides* 15(5): 967-983.
<https://doi.org/10.1007/s10346-018-0960-x>
- Fan X, van Westen CJ, Xu Q, et al. (2012) Analysis of landslide dams induced by the 2008 Wenchuan earthquake. *J Asian Earth Sci* 57: 25-37.
<https://doi.org/10.1016/j.jseaes.2012.06.002>
- Gorum T, Fan X, van Westen CJ, et al. (2011) Distribution pattern of earthquake-induced landslides triggered by the 12 May 2008 Wenchuan earthquake. *Geomorphology* 133(3-4): 152-167. <https://doi.org/10.1016/j.geomorph.2010.12.030>
- Gorum T, Van Westen CJ, Korup O, et al. (2013) Complex rupture mechanism and topography control symmetry of mass-wasting pattern, 2010 Haiti earthquake. *Geomorphology* 184: 127-138.
- Guzzetti F, Mondini AC, Cardinali M, Fiorucci F, Santangelo M, Chang KT (2012) Landslide inventory maps: New tools for an old problem. *Earth-Sci Rev* 112(1-2): 42-66.
<https://doi.org/10.1016/j.earscirev.2012.02.001>
- Guo D, Hamada M (2013) Qualitative and quantitative analysis on landslide influential factors during Wenchuan earthquake: a case study in Wenchuan County. *Eng Geol* 152(1): 202-209.
<https://doi.org/10.1016/j.enggeo.2012.10.012>
- Harp EL, Keefer DK, Sato HP, et al. (2011) Landslide inventories: the essential part of seismic landslide hazard analyses. *Eng Geol* 122(1-2): 9-21.
<https://doi.org/10.1016/j.enggeo.2010.06.013>
- Huang R, Fan X (2013) The landslide story. *Nat. Geos.* 6(5): 325-326. <https://doi.org/10.1038/ngeo1806>
- Huang R, Wang Y, Wang S, et al. (2011) High geo-stress distribution and high geo-stress concentration area models for eastern margin of Qinghai-Tibet plateau. *Sci China Technol Sc* 54(1): 154-166.
<https://doi.org/10.1007/s11431-011-4652-1>
- IEF - Institute of earthquake forecasting, CEA (2022a) Preliminary results of inversion of source rupture process of Ms 6.8 earthquake.
<https://www.ief.ac.cn/kydts/info/2022/69528.html>
- IEF - Institute of earthquake forecasting, CEA (2022b) Monitoring coseismic deformation of of 2022 Ms 6.8 Luding earthquake.
<https://www.ief.ac.cn/kydts/info/2022/69552.html>
- IEF - Institute of earthquake forecasting, CEA (2022c) Theoretical coseismic deformation of 2022 Ms 6.8 Luding earthquake.
<https://www.ief.ac.cn/kydts/info/2022/69544.html>
- Kargel JS, Leonard GJ, Shugar DH, et al. (2016) Geomorphic and geologic controls of geohazards induced by Nepal's 2015 Gorkha earthquake. *Science* 351(6269): aac8353.
<https://doi.org/10.1126/science.aac8353>
- Jeandet L, Steer P, Lague D, et al. (2019) Coulomb mechanics and relief constraints explain landslide size distribution. *Geophys Res Lett* 46(8): 4258-4266.
<https://doi.org/10.1029/2019GL082351>
- Jia D, Li Y, Lin A, et al. (2010) Structural model of 2008 Mw 7.9 Wenchuan earthquake in the rejuvenated Longmen Shan thrust belt, China. *Tectonophysics* 491(1-4): 174-184.
<https://doi.org/10.1016/j.tecto.2009.08.040>
- Keefer DK (1984) Landslides caused by earthquakes. *Geol Soc Am Bull* 95(4): 406-421. [https://doi.org/10.1130/0016-7606\(1984\)95<406:LCBE>2.0.CO;2](https://doi.org/10.1130/0016-7606(1984)95<406:LCBE>2.0.CO;2)
- Keefer DK (1994) The importance of earthquake-induced landslides to long-term slope erosion and slope-failure hazards in seismically active regions. *Geomorphology* 10(1-4): 265-284.
<https://doi.org/10.1016/B978-0-444-82012-9.50022-0>
- Keefer DK (2002) Investigating landslides caused by earthquakes-a historical review. *Surv Geophys* 23(6): 473-510.
- Ling S, Sun C, Li X, et al. (2021) Characterizing the distribution pattern and geologic and geomorphic controls on earthquake-triggered landslide occurrence during the 2017 Ms 7.0 Jiuzhaigou earthquake, Sichuan, China. *Landslides* 18(4): 1275-1291. <https://doi.org/10.1007/s10346-020-01549-6>
- Luo Y, Del Gaudio V, Huang, R, et al. (2014) Evidence of hillslope directional amplification from accelerometer recordings at Qiaozhuang (Sichuan—China). *Eng Geol* 183: 193-207. <https://doi.org/10.1016/j.enggeo.2014.10.015>
- Marc O (2016) Earthquake-induced landsliding. University at Potsdam, Doctoral Thesis.
- Marc O, Meunier P, Hovius N (2017) Prediction of the area affected by earthquake-induced landsliding based on seismological parameters. *Nat Hazard Earth Syst* 17(7): 1-15.
<https://doi.org/10.5194/nhess-17-1159-2017>
- Medwedeff WG, Clark MK, Zekkos D, et al. (2020) Characteristic landslide distributions: an investigation of landscape controls on landslide size. *Earth Planet Sci. Lett* 116203. <https://doi.org/10.1016/j.epsl.2020.116203>
- Meunier P, Hovius N, Haines AJ (2007) Regional patterns of earthquake - triggered landslides and their relation to ground motion. *Geophys Res Lett* 34(20).
<https://doi.org/10.1029/2007GL031337>
- Owen LA, Kamp U, Khattak GA, et al. (2008) Landslides triggered by the 8 October 2005 Kashmir earthquake. *Geomorphology* 94(1-2): 1-9.
<https://doi.org/10.1016/j.geomorph.2007.04.007>
- Papadimitriou E, Wen X, Karakostas V, et al. (2004) Earthquake triggering along the Xianshuihe fault zone of western Sichuan, China. *Pure Appl Geophys* 161(8): 1683-1707. <https://doi.org/10.1007/s00024-003-2471-4>
- Parker RN, Densmore AL, Rosser NJ, et al. (2011) Mass wasting triggered by the 2008 Wenchuan earthquake is greater than orogenic growth. *Nat Geosci* 4(7): 449-452.
<https://doi.org/10.1038/ngeo1154>
- Pradhan B, Singh RP, Buchroithner MF (2006) Estimation of stress and its use in evaluation of landslide prone regions using remote sensing data. *Adv Space Res* 37(4): 698-709.
<https://doi.org/10.1016/j.asr.2005.03.137>
- Ran Y, Chen L, Chen J, et al. (2010) Paleoseismic evidence and repeat time of large earthquakes at three sites along the Longmenshan fault zone. *Tectonophysics* 491(1-4): 141-153.
<https://doi.org/10.1016/j.tecto.2010.01.009>
- Ran Y, Chen L, Cheng J, et al. (2008) Late Quaternary surface deformation and rupture behavior of strong earthquake on the segment north of Mianning of the Anninghe fault. *Sci China Ser D* 51(9): 1224-1237.
<https://doi.org/10.1007/s11430-008-0104-6>
- Ren JJ, Xu XW, Zhang SM, et al. (2017) Tectonic transformation at the eastern termination of the Eastern Kunlun fault zone and seismogenic mechanism of the 8 August 2017 Jiuzhaigou M S 7.0 earthquake. *Chinese J Geophys* 60(10): 4027-4045.
<https://doi.org/10.6038/cjg20171029>
- Ren Z, Zhang Z, Dai F, et al. (2014) Topographic changes due to the 2008 Mw 7.9 Wenchuan earthquake as revealed by the differential DEM method. *Geomorphology* 217: 122-130.
<https://doi.org/10.1016/j.geomorph.2014.04.020>
- Roback K, Clark MK, West AJ, et al. (2018) The size, distribution, and mobility of landslides caused by the 2015 Mw7. 8 Gorkha earthquake, Nepal. *Geomorphology* 301: 121-138. <https://doi.org/10.1016/j.geomorph.2017.01.030>
- Stein S, Wysession M (2009) An introduction to seismology, earthquakes, and earth structure. John Wiley & Sons.
- Sun K, Meng G, Hong S, et al. (2021) Interseismic movement along the Luhuo-Daofu section of the Xianshuihe Fault from InSAR and GPS observations. *Chin J Geophys* 64(7): 2278-2296. <https://doi.org/10.6038/cjg202100364>
- Tang C, Ma G, Chang M, et al. (2015) Landslides triggered by the 20 April 2013 Lushan earthquake, Sichuan province,

- China. *Eng Geol* 187: 45-55.
<https://doi.org/10.1016/j.enggeo.2014.12.004>
- Tanyaş H, Van Westen CJ, Allstadt KE, et al. (2017) Presentation and analysis of a worldwide database of earthquake - induced landslide inventories. *J Geophys Res Earth* 122(10): 1991-2015.
<https://doi.org/10.1002/2017JF004236>
- Tanyaş H, van Westen CJ, Allstadt KE, et al. (2019) Factors controlling landslide frequency-area distributions. *Earth Surf. Proc. Land.* 44(4): 900-917.
<https://doi.org/10.1002/esp.4543>
- Tebbens SF (2020) Landslide scaling: a review. *Earth Space Sci* 7(1): e2019EA000662.
<https://doi.org/10.1029/2019EA000662>
- Tian Y, Xu C, Ma S, et al. (2019) Inventory and spatial distribution of landslides triggered by the 8th August 2017 MW 6.5 Jiuzhaigou earthquake, China *J Earth Sci* 30(1): 206-217. <https://doi.org/10.1007/s12583-018-0869-2>
- Valagussa A, Marc O, Frattini P, et al. (2019) Seismic and geological controls on earthquake-induced landslide size. *Earth Planet Sc Lett* 506: 268-281.
<https://doi.org/10.1016/j.epsl.2018.11.005>
- Wang H, Ran Y, Li Y, et al. (2014) A 3400-year-long paleoseismologic record of earthquakes on the southern segment of Anninghe fault on the southeastern margin of the Tibetan Plateau. *Tectonophysics* 628: 206-217.
<https://doi.org/10.1016/j.tecto.2014.04.040>
- Wang H, Wright TJ, Biggs J (2009) Interseismic slip rate of the northwestern Xianshuihe fault from InSAR data. *Geophys Res Lett* 36(3). <https://doi.org/10.1029/2008GL036560>
- Wang J, Howarth JD, McClymont EL, et al. (2020) Long-term patterns of hillslope erosion by earthquake-induced landslides shape mountain landscapes. *Sci Adv* 6(23): eaaz6446. <https://doi.org/10.1126/sciadv.aaz6444>
- Wang M, Shen ZK, Wang YZ, et al. (2021) Postseismic deformation of the 2008 Wenchuan earthquake illuminates lithospheric rheological structure and dynamics of eastern Tibet. *J Geophys Res Sol Ea* 126(9): e2021JB022399.
<https://doi.org/10.1029/2021JB022399>
- Wang YS, Li WG, Huang RQ, et al. (2007). The unloaded and relaxed phenomena in the valley bottom of the Daduhe River and its genetic mechanism. *J Chengdu Univ Technol* 34(4):379-383. (In Chinese with English Abstract)
- Wang Y, Wu LZ, Gu J (2019) Process analysis of the Moxi earthquake-induced Lantianwan landslide in the Dadu River, China. *B Eng Geol Environ* 78(7): 4731-4742.
<https://doi.org/10.1007/s10064-018-01438-2>
- Wang YS, Wu JF, Luo YH, et al. (2012) Seismic landslides and the environmental impact in the middle reach of Daduhe river. *Adv Mater Res* 368:1965-1970. <https://doi.org/10.4028/www.scientific.net/AMR.368-373.1965>
- Wu JF (2013) Research on development characteristics and genetic mechanism of the seismic landslide in Dadu River. Ph D thesis, Chengdu University of Technology, Chengdu, China. (In Chinese)
- Xu C (2015). Preparation of earthquake-triggered landslide inventory maps using remote sensing and GIS technologies: Principles and case studies. *Geosci Front* 6(6): 825-836.
<https://doi.org/10.1016/j.gsf.2014.03.004>
- Xu C, Xu X (2014b). Statistical analysis of landslides caused by the Mw 6.9 Yushu, China, earthquake of April 14, 2010. *Nat Hazards* 72(2): 871-893.
<https://doi.org/10.1007/s11069-014-1038-2>
- Xu C, Xu X, Yao X, et al. (2014a). Three (nearly) complete inventories of landslides triggered by the May 12, 2008 Wenchuan Mw 7.9 earthquake of China and their spatial distribution statistical analysis. *Landslides* 11(3): 441-461.
<https://doi.org/10.1007/s10346-013-0404-6>
- Xu C, Xu X, Shyu JBH (2015) Database and spatial distribution of landslides triggered by the Lushan, China Mw 6.6 earthquake of 20 April 2013. *Geomorphology* 248: 77-92.
<https://doi.org/10.1016/j.geomorph.2015.07.002>
- Xu C, Xu X, Shyu JBH, et al. (2014b) Landslides triggered by the 22 July 2013 Minxian-Zhangxian, China, Mw 5.9 earthquake: inventory compiling and spatial distribution analysis. *J Asian Earth Sci* 92: 125-142.
<https://doi.org/10.1016/j.jseae.2014.06.014>
- Xu Q, Fan XM, Huang RQ, et al. (2009) Landslide dams triggered by the Wenchuan Earthquake, Sichuan Province, south west China. *B Eng Geol Environ* 68(3): 373-386.
<https://doi.org/10.1007/s10064-009-0214-1>
- Xu X, Wen X, Yu G, et al. (2009) Coseismic reverse-and oblique-slip surface faulting generated by the 2008 Mw 7.9 Wenchuan earthquake, China. *Geology* 37(6): 515-518.
<https://doi.org/10.1130/G25462A.1>
- Xu X, Wen X, Han Z, et al. (2013) Lushan Ms 7.0 earthquake: a blind reserve-fault event. *Chinese Sci Bull* 58(28): 3437-3443.
<https://doi.org/10.1007/s11434-013-5999-4>
- Yuan RM, Deng QH, Cunningham D, et al. (2013) Density distribution of landslides triggered by the 2008 wenchuan earthquake and their relationships to peak ground acceleration. *B Seismol Soc Am* 103(4): 2344-2355.
<https://doi.org/10.1785/0120110233>
- Zhao B (2020) The Mechanism of Large Earthquake-Triggered Landslides in Area of High Intensity and Deep Canyon of Northwest Sichuan. Chengdu University of Technology, Doctoral Thesis. (In Chinese)
- Zhao B (2021) Landslides triggered by the 2018 Mw 7.5 Palu supershear earthquake in Indonesia. *Eng Geo* 294: 106406.
<https://doi.org/10.1016/j.enggeo.2021.106406>
- Zhao B, Huang Y, Zhang C, et al. (2015) Crustal deformation on the Chinese mainland during 1998-2014 based on GPS data. *Geod Geodyn* 6(1): 7-15.
<https://doi.org/10.1016/j.geog.2014.12.006>
- Zhao B, Li W, Su L, et al. (2022b) Insights into the Landslides Triggered by the 2022 Lushan Ms 6.1 Earthquake: Spatial Distribution and Controls. *Remote Sens* 14(17): 4365.
<https://doi.org/10.3390/rs14174365>
- Zhao B, Liao H, Su L (2021a) Landslides triggered by the 2018 Lombok earthquake sequence, Indonesia. *Catena* 207: 105676.
<https://doi.org/10.1016/j.catena.2021.105676>
- Zhao B, Wang Y, Feng Q, et al. (2020b) Preliminary analysis of some characteristics of coseismic landslides induced by the Hokkaido Iburi-Tobu earthquake (September 5, 2018), Japan. *Catena* 189: 104502.
<https://doi.org/10.1016/j.catena.2020.104502>
- Zhao B, Wang Y, Li W, et al. (2021b) Insights into the geohazards triggered by the 2017 Ms 6.9 Nyingchi earthquake in the east Himalayan syntaxis, China. *Catena* 205: 105467.
<https://doi.org/10.1016/j.catena.2021.105467>
- Zhao B, Wang YS, Luo YH, et al. (2018) Landslides and dam damage resulting from the Jiuzhaigou earthquake (8 August 2017), Sichuan, China. *Roy Soc Open Sci* 5(3): 171418.
<https://doi.org/10.1098/rsos.171418>
- Zhao B, Wang YS, Su LJ, et al. (2020a) Directional seismic response to the complex topography: A case study of 2013 Lushan Ms 7.0 earthquake. *J Mt Sci* 17(9): 2049-2067.
<https://doi.org/10.1007/s11629-020-6038-y>
- Zhao B, Wang Y, Li W, et al. (2022a). Evaluation of factors controlling the spatial and size distributions of landslides, 2021 Nippes earthquake, Haiti. *Geomorphology* 108419.
<https://doi.org/10.1016/j.geomorph.2022.108419>
- Zhao B, Wang Y, Wu J, et al. (2021c) The Mogangling giant landslide triggered by the 1786 Moxi M 7.75 earthquake, China. *Nat Hazards* 106(1): 459-485.
<https://doi.org/10.1007/s11069-020-04471-1>
- Zhao ZJ, Liu Y, Chen Y, et al. (2013) Quaternary fluvial incision rates of the Western Sichuan Plateau inferred from ESR chronology. *J Lanzhou Univ* 49(2): 160-165. (In Chinese)